Geophysical Journal International

Geophys. J. Int. (2016) **204,** 418–439
GJI Seismology

doi: 10.1093/gji/ggv444

Seismic response of a deep continental basin including velocity inversion: the Sulmona intramontane basin (Central Apennines, Italy)

Giuseppe Di Giulio,[1] Rita de Nardis,[2,4] Paolo Boncio,[2] Giuliano Milana,[3] Gianluigi Rosatelli,[2] Francesco Stoppa[2] and Giusy Lavecchia[2]

[1]*Istituto Nazionale di Geofisica e Vulcanologia, Section Roma1, Seismology and Tectonophysics, Via Arcivescovado* 8, *I*-67100, *L'Aquila, Italy. E-mail: giuseppe.digiulio@ingv.it*
[2]*University of Chieti-Pescara "G. d'Annunzio", DiSPUTer, Via dei Vestini* 30, *I*-66100, *Chieti Scalo (CH), Italy*
[3]*Istituto Nazionale di Geofisica e Vulcanologia, Section Roma1, Seismology and Tectonophysics, Via di Vigna Murata* 605, *I*-00143, *Rome, Italy*
[4]*Dipartimento della Protezione Civile, Via Vitorchiano* 2, *I*-00189 *Rome, Italy*

Accepted 2015 October 12. Received 2015 June 15; in original form 2014 December 29

SUMMARY

The Sulmona plain (central Italy) is an intramontane basin of the Abruzzi Apennines that is known in the literature for its high seismic hazard. We use extensive measurements of ambient noise to map the fundamental frequency and to detect the presence of geological heterogeneities in the basin. We perform noise measurements along two basin-scale orthogonal transects, in conjunction with 2-D array experiments in specific key areas. The key areas are located in different positions with respect to the basin margins: one at the eastern boundary (fault-controlled basin margin) and one in the deepest part of the basin. We also collect independent data by using active seismic experiments (MASW), down-hole and geological surveys to characterize the near-surface geology of the investigated sites.

In detail, the H/V noise spectral ratios and 2-D array techniques indicate a fundamental resonance (f_0) in the low-frequency range (0.35–0.4 Hz) in the Sulmona Basin. Additionally, our results highlight the important role that is played by the alluvial fans near the edge-sectors of the basin, which are responsible for a velocity inversion in the uppermost layering of the soil profile. The H/V ratios and the dispersion curves of adjacent measurements strongly vary over a few dozens of meters in the alluvial fan area. Furthermore, we perform 1-D numerical simulations that are based on a linear-equivalent approach to estimate the site response in the key areas, using realistic seismic inputs. Finally, we perform a 2-D simulation that is based on the spectral element method to propagate surface waves in a simple model with an uppermost stiff layer, which is responsible for the velocity inversion. The results from the 2-D modelling agree with the experimental curves, showing deamplified H/V curves and typical shapes of dispersion curves of a not normally dispersive site.

Key words: Fourier analysis; Earthquake ground motions; Site effects.

1 INTRODUCTION

Investigating basin effects is of primary importance for the evaluation and mitigation of seismic risk. Urbanized and industrial areas are often located within sediment-filled basins, where ground motion amplification can be very large in terms of the amplitude and signal duration. Aggravations of seismic effects on buildings that are situated in basins have been evidenced through experimental and modelling studies (Makra *et al.* 2001; Semblat *et al.* 2005; Stupazzini *et al.* 2009b; Chaljub *et al.* 2010 among many others). Following the work of Bard & Bouchon (1980a,b, 1985), who used numerical modelling, the occurrence of 1-D site effects or 2-D/3-D resonance amplification within alluvial valleys depends on both (i) the basin's geometry (shape ratio), and (ii) the velocity contrast between the sediments and bedrock. In shallow valleys, 1-D stratigraphic amplification is often combined to the lateral propagation of surface waves that are generated from the basin's edges. The reflection and scattering of seismic waves near the edges considerably increase the duration of ground motion (Bindi *et al.* 2009; Cara *et al.* 2011). For moderate or strong earthquakes, basin effects can also be responsible for a relatively narrow damaged zone that is located close (but not coincident) to the basin's edge (Gao *et al.* 1996; Kawase 1996). In deep valleys, 2-D resonant modes of SH and P-SV waves are also possible, with 2-D resonances occurring at different frequencies from those of 1-D resonant modes (Steimen *et al.* 2003; Roten *et al.* 2006).

Seismic procedures, such as microzonation and site effects analyses, widely use H/V spectral noise ratios (Nakamura 1989) and surface-wave methods (Tokimatsu 1997). Generally, a common simplified practice during site response analysis is to assume simplified soil profiles that show a velocity function that increase with depth (i.e. normally dispersive site). When a significant velocity reversal is present in the geological structure, the Italian seismic code (NTC 2008) recommends more accurate studies to perform numerical modelling of the site response.

To investigate the seismic response in a complex geological context (i.e. deep basin characterized by basin-edge complexities), we choose an area with these characteristics and a high seismic hazard, namely, the Sulmona plain in central Italy. The Sulmona plain and its surrounding areas are quite urbanized (e.g. the city of Sulmona has approximately 25000 citizens); consequently, the seismic risk level of the whole zone is significantly high. The Sulmona Basin was also recently selected as a near-fault test site to perform 3-D ground motion predictions. Faccioli *et al.* (2008), Stupazzini *et al.* (2009a) and Villani *et al.* (2013) applied a spectral element code (called GeoELSE; Stupazzini 2004) to assess the seismic hazard of this area creating shaking scenarios. These authors selected a realistic M_w 6.4 event and allowed some parameters (hypocentre location, slip distribution, rupture velocity and rake angle) to vary. An Empirical Green's Function method (Ordaz *et al.* 1995) and a stochastic approach (Boore 2003) were also adopted to enhance the frequency content of the simulations (up to 2.5 Hz). These simulations found that the unfavourable interactions between fault rupture, radiation mechanisms and complex geological conditions may give rise to large peak ground velocity values (exceeding 1 m s^{-1}), which considerably increase the seismic risk of the area. However, these simulations had poor knowledge of the dynamic properties of the infilling sediments and of the local geometry within the basin; for example, these simulations do not consider the velocity inversion in the *Vs* profile due to the presence of alluvial fans or fluvial gravels on top of fine-grained lacustrine deposits (e.g. Di Capua *et al.* 2009). This last feature is quite common in the intra-Apennine continental basins of central Italy. Thus investigating with experimental and numerical analyses the role played by a velocity inversion on the H/V and dispersion curves is of increasing interest. Such effects on the H/V curves have been recently discussed by Castellaro & Mulargia (2009a,b). By using field observations and 1-D models, these authors documented that a rigid layer that superimposes a soft layer causes a depression in the noise Fourier Amplitude Spectra (FAS), mainly on the horizontal components of the noise wavefield. A decrease in the horizontal FAS below the vertical one provides H/V noise ratio with persistent amplitudes that are lower than 1 in a wide frequency band.

Moreover, velocity inversion in a subsoil profile significantly affects surface wave dispersion curves. A seismic velocity inversion causes a signature on the measured dispersion curves, with the possibility of mode jumps and multiple higher modes that are difficult to identify properly (e.g. Forbriger 2003). In such a situation, the inversion of the field curves is critical due to the problem of the non-uniqueness of the solution (Wathelet 2005; Di Giulio *et al.* 2012).

In this paper, we derive a 2-D subsurface structure of the investigated area. We evaluate the seismic response of the deep Sulmona Basin that is characterized by velocity inversion, highlighting the potentiality and limit of noise and array techniques. The first part of the paper is devoted to describe the results of (i) extensive H/V noise measurements along two main orthogonal transects at the basin scale, and of (ii) specific investigations in two key areas that are located at the eastern border (*Badia Morronese*) and in the deepest part of the basin (*San Pelino - Raiano*). We acquired new near-surface geological information, geophysical (MASW, downhole and noise surveys) and geotechnical data (shear modulus and damping ratio of soil from laboratory tests) at these key sites. The results are used to better constrain the local shear wave velocity (*Vs*) profiles, and to reconstruct the geological models of the key sites.

The second part of the paper is based on the 1-D and 2-D numerical modelling of the site response, including the effect of the velocity inversion within the soil profile. Specifically, the 1-D modelling (through a linear equivalent approach; Bardet *et al.* 2000) takes into account realistic seismic inputs and the *Vs* profile up to the seismic bedrock, as retrieved from the surface wave analysis. 1-D models reproduce the seismic response in terms of the acceleration response spectra at the key sites, indicating a different level of seismic amplification that is also related to the presence of a superficial stiff layer. The 2-D numerical computation, using a spectral element method (http://www.geodynamics.org/cig/software/specfem2d; Komatitsch & Tromp 1999; Chaljub 2006), analyses the effect on the H/V and dispersion curves of a velocity inversion that is present in the uppermost layer. The 2-D computations provide synthetics that give deamplified H/V curves when the near-surface profile is characterized by a significant reversal of velocity, which agrees with the experimental curves.

2 GEOLOGICAL AND SEISMOTECTONIC SETTING

The Sulmona Basin (Fig. 1) is located in the central-eastern part of the Abruzzi Apennines (central Italy), a Late Miocene–Early

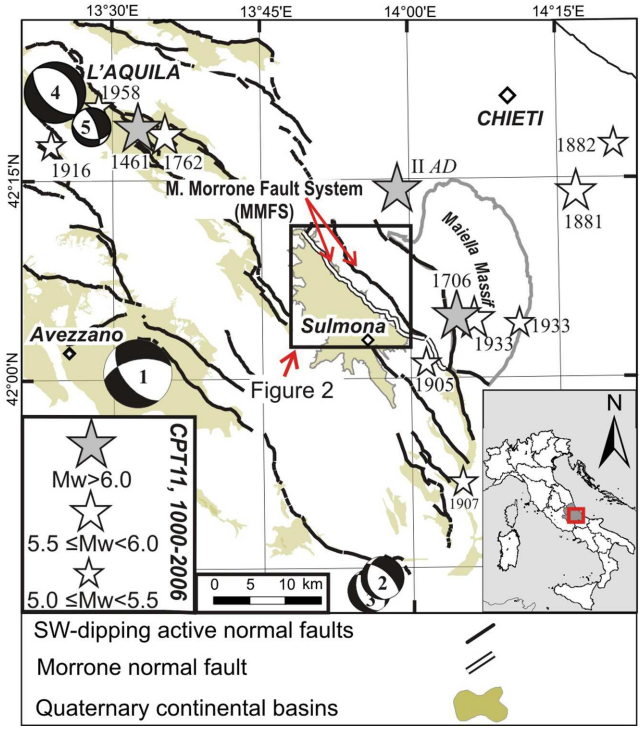

Figure 1. Map of the active faults and the focal mechanisms of the $M_w \geq 5.5$ earthquakes in the central Apennines. 1 – Avezzano 1915 (M_s 6.9; Amoruso *et al.* 1998); 2, 3 – Barrea 1984 (M_w 5.9, M_w 5.5; Pondrelli *et al.* 2006); 4 – L'Aquila 2009 April 6 (M_w 6.3; Pondrelli *et al.* 2010); 5 – L'Aquila 2009 April 7 (M_w 5.5; Pondrelli *et al.* 2010). The stars indicate historical events (Ceccaroni *et al.* 2009; Rovida *et al.* 2011).

Figure 2. Geological map of the Sulmona Basin (simplified from Carta Geologica d'Italia 2005 with the locations of the basin-scale transects (*AA′*, *BB′*) and horizontal-to-vertical noise spectral ratio measurements (white triangles). The depth of the gravimetric bedrock is from Miccadei *et al.* (1998). The squares indicate the location of the two key areas: *San Pelino* (*SP*) and *Badia Morronese* (*BM*).

Pliocene fold and thrust belt post-dated by Quaternary extensional tectonics. This extension in the area produced normal faults with dip-slip to normal-oblique kinematics, which strike NW–SE on average and mainly dip to the SW, thus controlling the formation of intramontane depressions. Active extension is proven by upper crust instrumental seismicity, geodetic data, and integrated geological–seismological stress data (Boncio *et al.* 2010; D'Agostino *et al.* 2011; Lavecchia *et al.* 2012; Ferrarini *et al.* 2014).

The Sulmona plain is one of the largest tectonic depressions in the central Apennines (Figs 1 and 2). It is a half-graben that is bounded on the eastern side by the SW-dipping *Mt. Morrone Fault System* (*MMFS* in Fig. 1). The basin extends for 17–18 km along the *MMFS* and for 5–8 km perpendicular to it. The basin is filled by clastic continental deposits, which have a maximum estimated thickness of ~450 m based on available gravimetric and seismic reflection data and a hypothetical depocentral area between *Badia Morronese* and *Corfinio* (Fig. 2; Miccadei *et al.* 1998, 2002). No direct constraints exist on the lithology and the age of the oldest continental deposits that fill the deepest part of the basin. The oldest outcropping sediments are Lower Pleistocene slope-derived breccias that hang on the western (*Vittorito* village) and eastern (footwall of *MMFS*) slopes of the basin, and probably interfinger with

lacustrine sediments in the subsurface of the central part of the basin. The upper part of the continental succession is constrained by borehole and field data, and consists of Lower-to-Middle Pleistocene fine-grained lacustrine deposits (clay and carbonate silt), passing upwards to coarse-grained Upper Pleistocene fluvial or alluvial fan sediments (Miccadei *et al.* 1998; Giaccio *et al.* 2012).

The *MMFS* consists of two major nearly parallel segments that are spaced 2–3 km apart in map view (Fig. 1), and have a total length of 22–23 km along strike (Gori *et al.* 2011). Both fault segments have an average dip of 50° and a slightly oblique left-lateral kinematics. The eastern segment offsets a folded Mesozoic carbonate sequence along the south-western limb of the *Mt. Morrone* anticline; the western segment runs along the eastern side of the Sulmona Basin. Based on morphotectonic and palaeoseimological evidence, the western segments cut Late Pleistocene and Holocene alluvial fan and slope deposits, with an average minimum late Quaternary slip rate ranging from 0.4 to 0.8 mm yr^{-1}. The maximum magnitude associated to the *MMFS* has been estimated to be on the order of 6.5–6.7 (Galadini & Galli 2000; Boncio *et al.* 2004; Gori *et al.* 2011; Galli *et al.* 2015). Despite geological evidence of ongoing extension, the Sulmona plain remained almost aseismic in instrumental times, with a very low level of background seismicity compared to surrounding areas (de Nardis *et al.* 2011; Romano *et al.* 2013). Conversely, some major historical earthquakes are located in the surrounding areas of the Sulmona Basin (Guidoboni *et al.* 2007; Rovida *et al.* 2011), including earthquakes in the II century A.D. (M_w 6.6-6.7), November 1706 (I_o X/XI MCS, M_w 6.8), and September 1933 (I_o IX MCS, M_w 6.0). Based on archaeoseismological data, Ceccaroni *et al.* (2009) associated the II century A.D. event to the activity of the *MMFS*. Lavecchia & de Nardis (2009) related the 1706 and 1933 earthquakes to the activity of the SW-dipping regional basal thrust (Abruzzo Citeriore Basal Thrust in de Nardis *et al.* 2011), which is located eastward compared to the *MMFS* and at probable depths of 15–20 km beneath the Sulmona plain. The *MMFS* remained silent for a long time, with evident implications in terms of time-dependent seismic hazard. This is further confirmed by Galli *et al.* (2015), who found palaeoseismologic evidence for average recurrence times of ∼2400 yr on the *MMFS*, with the last large earthquake occurring during the II century A.D., which agrees with archaeoseismological data (Ceccaroni *et al.* 2009).

3 AMBIENT VIBRATION DATA ALONG BASIN-SCALE TRANSECTS

Measurements of H/V noise spectral ratios, in conjunction with independent information, are a suitable tool to investigate the geological structure of deep and complex basins (Uebayashi 2003; Bonnefoy-Claudet *et al.* 2009). H/V curves, which are computed in terms of the FAS ratio between the horizontal and vertical components of ambient noise vibrations, can be used in a first approximation to indicate the strength of the impedance contrast between soft sediment layers and bedrock.

To better define the deep geometry of the Sulmona Basin, we collected ambient noise measurements along two orthogonal transects that are approximately 10 and 5 km long, respectively (section AA′ and BB′ in Fig. 2). The average station spacing is on the order of 500 m. The 34 noise measurements are sited at (1) rock sites at the ends of both transects, (2) sites with thick layers of soft continental deposits, and (3) sites in the basin that have important historical monuments. The *AA′* section starts from *Vittorito* village (Fig. 2), approaches the *Corfinio* village and ends near the *Badia Morronese* village. The *BB′* section stretches from *Raiano* village to *Roccacasale* village (Fig. 2). The historical abbeys of *San Pelino* (*SP*) and *Badia Morronese* (*BM*), which are the two key sites that are investigated in detail in this study, are located at the villages of *Corfinio* and *Badia Bagnaturo.* Ambient noise was recorded by using 24-bit Reftek130 data loggers that were coupled to Lennartz LE-3D5s velocimeters with an eigenfrequency of 0.2 Hz. The sampling rate was fixed at 250 Hz with a recording duration of at least 50 min.

The H/V ratio (Bard & SESAME-Team 2005) was computed by using 60 s time mobile windows, and an anti-trigger software was used to remove time windows that were affected by transients related to anthropic sources (www.geopsy.org). The FASs of each selected time window were smoothed with a Konno & Ohmachi filter (1998) that used a coefficient of 40. The horizontal amplitude spectra were computed by a quadratic mean between NS and EW components. Finally, the H/V ratio and the standard deviation were computed by a geometrical average of the H/V ratios from all the selected windows.

The H/V analysis shows a clear high-amplitude low-frequency peak at 0.35–0.5 Hz (Fig. 3), indicating a strong and deep impedance contrast in the Sulmona Basin. The strongest and narrower H/V peaks (centred at 0.37 Hz), which have a mean amplitude level of 8, are observed from *t01 to t11* measurements (northwest and southeast of the village of *Pratola Peligna* in *AA′* section, see Figs 2 and 3a_1). Broader H/V peaks (within 0.35-0.49 Hz) and lower amplitudes are observed from *t12* to *t15* (Fig. 3a_2) towards the eastern edge of the basin. These shapes could indicate complex site effects that are caused by body and surface waves that were diffracted from the geological heterogeneity. A secondary H/V peak is also evident for the *t12* (at 8–10 Hz) and the *t15* (at 6 Hz) sites (Fig. 3a_2), suggesting a possible secondary impedance contrast in the uppermost layers. *t16* and *t17* are on the eastern flank on fractured rocks (Fig. 2) in the footwall of the *MMFS* (approximately 700 m NE from the *Badia Morronese* abbey), and the respective H/V curves can be assumed as flat at least up to 5 Hz (Fig. 3a_3).

In the northern sector of the studied area, the noise measurements were situated on the carbonate bedrock, the lacustrine infill and the alluvial valleys of the Aterno and Sagittario rivers. The *sul01* site was located on rock outcrops (near the *Vittorito* village, see Fig. 2) and its H/V is almost flat, except at low frequencies, where an H/V bump is present (see Fig. 3b_1). At *sul02,* a weak H/V peak can be recognized at 1.3 Hz, whereas *sul03* shows a clear f_0 at 0.48 Hz (Fig. 3b_2). *sul04* and *tt05* show similar low-frequency H/V peaks that are centred at approximately 0.4 Hz (Fig. 3b_3). An increase in f_0, from 0.38 to 0.48 Hz with a consistent decrease in the amplitude level, is observed from the *tt05* to *tt02* sites, suggesting a thinning of the soft sediment layer along this part of the *BB′* section (Figs 3b_3, 3b_4 and 3b_5). The *tt01* and *tt00* sites are located on rock outcrops on the eastern flank of the basin (Fig. 2), and their H/V curves are almost flat (Fig. 3b_6). The remaining noise measurements along the *San Pelino-Raiano* direction are shown in Fig. 3(c). The t*18* site was likely affected by a low-frequency instrumental disturbance (Fig. 3c_1), *t19* and *t20* share a similar H/V shape with a clear resonance at 0.38 Hz (Fig. 3c_2), and the *t21* site (near *Raiano* village) shows an f_0 of 0.41 Hz (Fig. 3c_3).

It is worth noting that the H/V ratios often show H/V amplitudes that are lower than 1 in a large frequency band (i.e. Figs 3a_1, 3a_2, 3c_2 and 3c_3).

To summarize the results of the single-station noise measurements, the H/V curves in Fig. 3 were plotted as contour diagrams along the *AA′* and *BB′* geological sections (Fig. 4). The 2-D

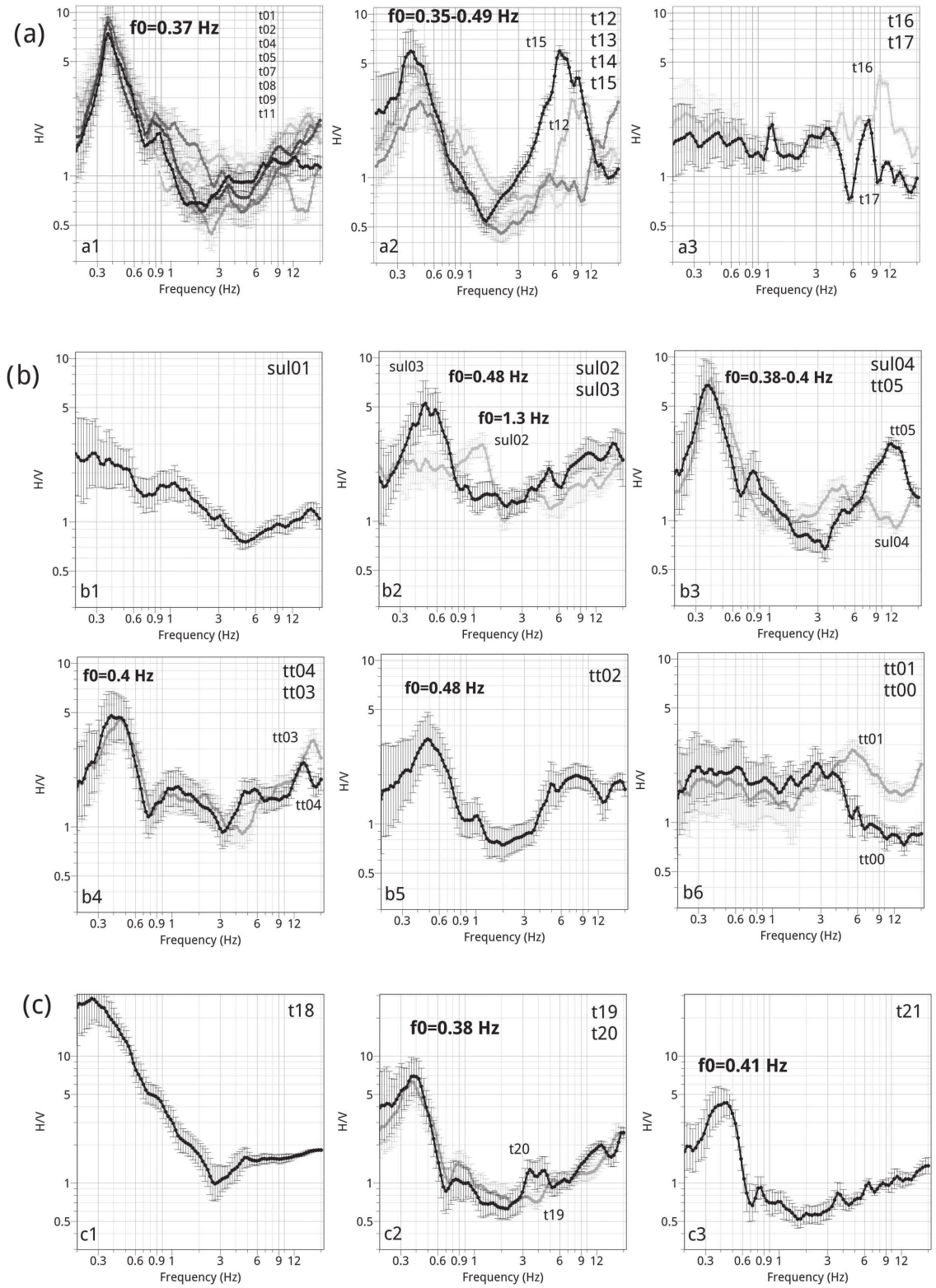

Figure 3. Average H/V curves (error bars show the standard deviation) for (a) the *Corfinio-Badia Morronese* section (*t01, t02, t04, t05, t07, t08, t09, t11, t12, t13, t14, t15, t16* and *t17* sites), (b) the *Vittorito-Roccacasale* section (*sul01*, *sul02*, *sul03*, *sul04*, *tt05*, *tt04*, *tt03*, *tt02*, *tt01* and *tt00* sites) and (c) the *Corfinio-Raiano* section (*t18*, *t19*, *t20* and *t21* sites).

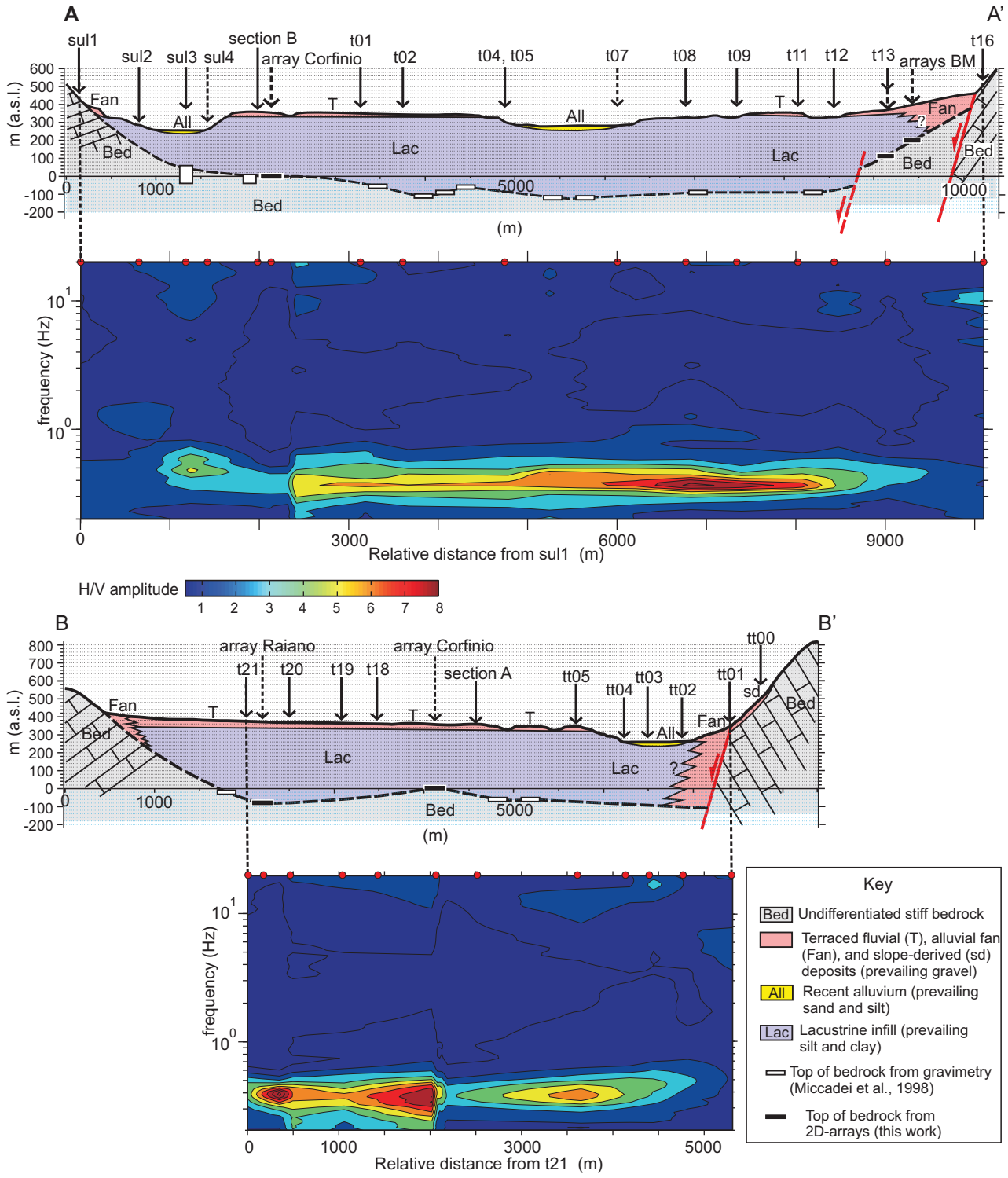

Figure 4. Geological sections *AA′* (top) and *BB′* (bottom) plotted with the H/V ratios contours (shown in Fig. 3). The geological sections were constructed after the geological and geophysical surveys described in the text, and by using *a priori* information on the bedrock depth from gravimetric data (Miccadei *et al.* 1998). The arrows on the geological sections and the red dots on the H/V contours represent the noise sites along the AA′ and BB′ transects (location in Fig. 2).

geological sections in Fig. 4 were constructed based on geological and geophysical surveys that were performed during this work, and by using independent information on the bedrock depth as provided by available gravimetric data (Miccadei *et al.* 1998).

4 MULTIDISCIPLINARY APPROACH ON KEY AREAS

In addition to the ambient noise measurements along the two transects (*AA′* and *BB′*), we focus our investigation on two sites (see

Fig. 2 for locations): the *Badia Morronese* abbey (hereafter *BM*, XIII century A.D., situated in the *Badia Bagnaturo* village), and the *San Pelino* abbey (hereafter *SP*, XI century A.D., situated in the *Corfinio* village). These two key sites are important from a historical-monumental point of view and for their locations within the basin. In fact, *BM* is located on the eastern side of the basin along the *AA′* section and is close to the fault-controlled basin margin. *SP* is located in the central part of the *BB′* section, where the top of the bedrock is deep and its geometry is not affected by significant elevation variations. Downhole and MASW surveys, and five small-aperture 2-D arrays of seismological stations were performed for the seismic characterization at these two sites. We also acquired constraints on the geotechnical model for the uppermost 40 m of the subsoil thanks to geognostic wells and laboratory tests on undisturbed samples.

4.1 Deep basin: *San Pelino abbey* (*Corfinio-Raiano* area)

4.1.1 Subsurface geological model

The villages of *Raiano* and *Corfinio* are located in the central-northern part of the Sulmona Basin (Fig. 2; *BB′* section of Fig. 4), where the continental deposits reach their maximum thickness (Di Filippo & Miccadei 1997; Miccadei *et al.* 1998). The two villages are built on Middle-to-Upper Pleistocene fluvial and alluvial fan deposits. The surface and subsurface geology of the *SP* area is synthesized in Fig. 5. The surface fluvial and alluvial fan deposits (*Ta1* in Fig. 5) mostly consists of thickly bedded, dense gravels with a sandy-silty matrix, containing decimetric interlayers of sands, silty sands, brownish palaeosols and epiclastic tephra. The gravel unit forms a laterally continuous, 10–20-m-thick (locally, up to 30-m-thick) layer that rests on fine-grained Lower-Middle Pleistocene lacustrine deposits (see geologic section in Fig. 5). The presence of a decametric layer of dense gravels capping fine-grained lacustrine deposits is a feature that is common to a large part of the Sulmona Basin. Based on borehole and field data, we distinguished two units within the lacustrine deposits (*La1* and *La2* in Fig. 5). The *La1* unit consists of grey, stiff clayey silt-to-silty clay with peat horizons and grey, dense sand. The *La2* unit consists of stratified, whitish-to-light grey, stiff carbonate silt with subordinate sand. Layers of gravel may be present within the fine-grained deposits at different stratigraphic positions. Overall, the total thickness of the continental deposits beneath the *SP* abbey, and in general beneath the *Corfinio-Raiano* area, is 350–400 m (see 2-D models in Fig. 5). Nevertheless, the total thickness from the ground surface may strongly vary laterally due to fluvial erosion (e.g. compare the northern and southern parts of the geologic section in Fig. 5). No direct constraints exist on the lithology of the bedrock, even though the bedrock likely consists of the Mesozoic carbonate rocks that outcrop north and west of the continental basin (Centamore *et al.* 2006).

The shallow subsurface stratigraphy was analysed in detail by a 40-m-deep geognostic well (S1 in Fig. 5). The borehole drilled ∼12 m of gravels in the *Ta1* unit, ∼9 m of sand, silt and gravel that were interpreted as the lower part of *Ta1*, and then ∼19 m of silt, clay and sand in the *La1* unit. An undisturbed sample of grey, clayey silt was cored within the *La1* unit for laboratory dynamic analyses (see Fig. S1 and Table S1 of the online supplementary material). A down-hole experiment that wes performed within the S1 well allowed us to measure the *Vs* within the *Ta1* gravels (values of 750–800 m s^{-1}), which indicated a sharp velocity inversion at the transition to the underlying finer material (*Vs* from 750–800 to 350–400 m s^{-1}); afterward, the *Vs* remained stable (∼350 m s^{-1}) up to depths of ∼30 m (Fig. 5).

4.1.2 2-D array: method and results

The arrays that were deployed in the key areas of the Sulmona Basin comprised 12 seismological stations approximately arranged on circular rings. The equipment was of the same typology used for the single-station noise measurements. Time synchronism was provided at each station by a GPS antenna. The sensor position was determined by GPS differential corrections that were measured by a Leica System 1200 GNSS instrument. The positioning error was on the order of a few centimetres. The noise data were recorded simultaneously at each array for approximately 1 hr and 30 min. The array analysis was performed by using the *geopsy* tool (www.geopsy.org). We applied classical (CVFK) and high-resolution frequency-wavenumber (HRFK) analysis (Capon 1969; Ohrnberger *et al.* 2004) on the vertical component to derive the apparent phase-velocity dispersion curves. The wavenumber limits, in terms of the resolution and aliasing effects, were selected by computing the theoretical array transfer function for each array, as described in Di Giulio *et al.* (2006) and Wathelet *et al.* (2008). We inverted the phase-velocity dispersion and the H/V curves to retrieve a *Vs* profile (Scherbaum *et al.* 2003), by using the neighbourhood algorithm (Sambridge 1999) as implemented by Wathelet (2008). In this approach, the H/V curve is theoretically related to the Rayleigh wave ellipticity of the fundamental mode (Fäh *et al.* 2001; Lunedei & Albarello 2010; Socco *et al.* 2010). Inversion in terms of the H/V curve was performed in this study by considering the H/V peak frequency that was assumed as the ellipticity peak of the Rayleigh waves, including also a selection of a portion of the experimental H/V curve around f_0. According to Hobiger *et al.* (2013), the branches of the actual H/V curve around f_0 can better constrain the inversion, especially the right-branch, which is the most reliable part of an ellipticity measurement. The amplitude of the H/V peak was not considered in our inversion because the peak value of an H/V curve is not reliable. In fact, the ellipticity of the fundamental mode of Rayleigh waves should theoretically have infinite amplitude at f_0 (purely horizontal polarization of Rayleigh waves).

Another important assumption in the inversion process is that the geometry of the subsoil is 1-D, with the interface between layers being planar (Renalier 2010). However, the assumption of predominant surface waves cannot be fully met in very stiff sites where the energetic role of surface waves is generally low, and in sites with a significant contribution from body waves in the wavefield (Endrun *et al.* 2010). Furthermore, even if the second assumption assumes a 1-D medium, several works in the literature use surface-wave inversion applied on a subset of instruments to reconstruct lateral variation in the *Vs* structure (Xia *et al.* 1999; Picozzi *et al.* 2009; Renalier *et al.* 2010). The experimental dispersion curves for all the target sites in the basin, which are summarized in Fig. 6, suggest the presence of some velocity inversion (i.e. not normally dispersive site) because the apparent phase-velocity does not always decrease with increasing frequency.

In detail for the *SP* area, we located two 2-D arrays of seismic stations around the abbey (Fig. 5) and one near the *Raiano* village (see Fig. 2 for location), allowing us to verify if an heterogeneity in the velocities was present along the *Corfinio-Raiano* direction. The two arrays around *SP* (*Cb* and *Cs* in Fig. 5) were characterized by different maximum apertures for investigating a wider range of frequencies. The smallest array (*Cs*) had a maximum aperture of

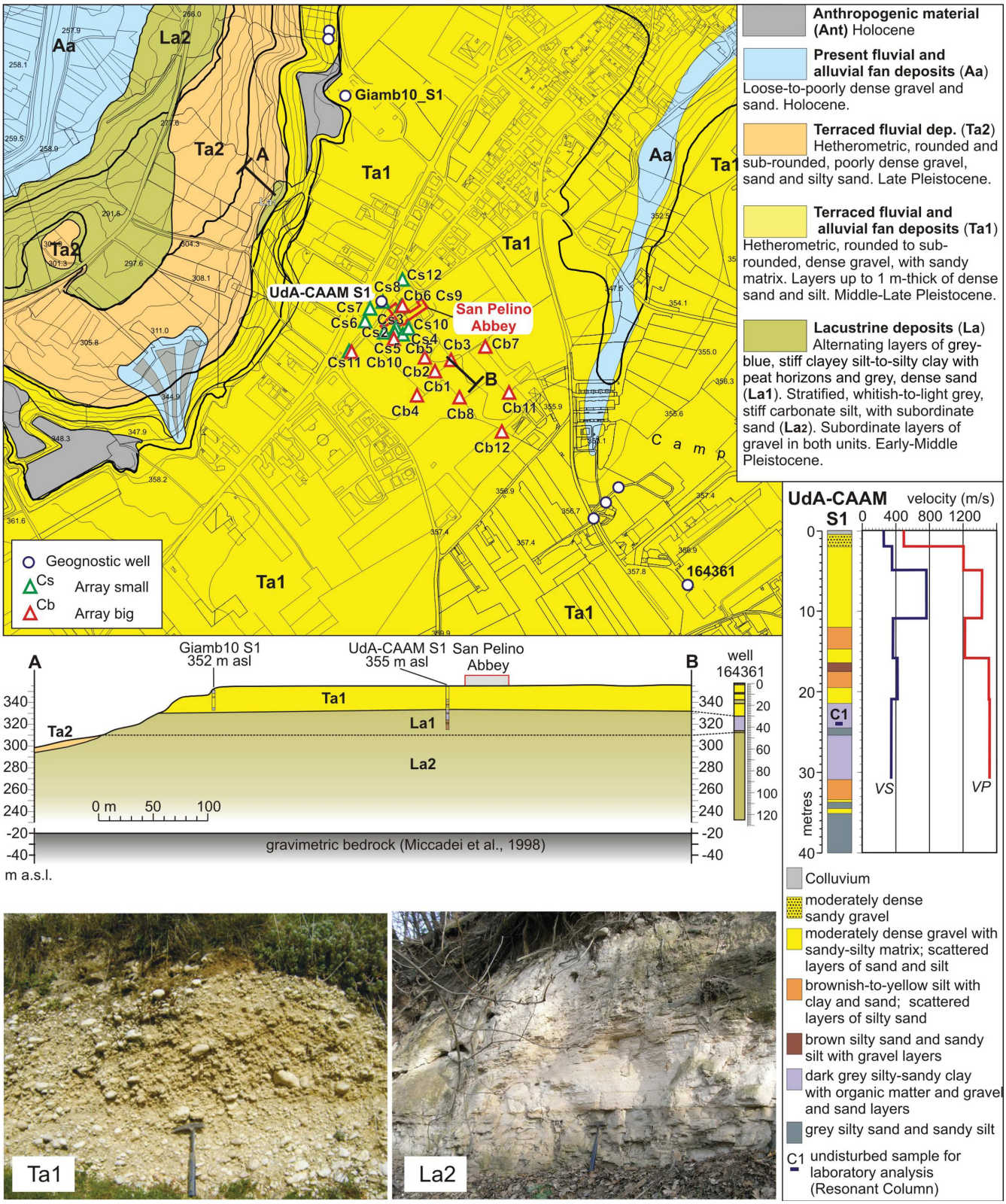

Figure 5. Geological map of the area surrounding the *San Pelino* abbey (*Corfinio*, location in Fig. 2). The pictures show the field view of the *Ta1* and *La2* units. The stratigraphy is also shown, with the *Vp* and *Vs* profiles (from down-hole experiment) of the geognostic well that was drilled in this study near the abbey.

100 m, whereas the biggest one (*Cb*) had a maximum aperture of 350 m with the configuration layout shown in Fig. 5. The mean H/V (Fig. 7a) and FAS curves (Figs 7b and c), which were obtained as geometrical averages among the stations in the *Cb* and *Cs* arrays, show a clear f_0 at 0.4 Hz. The only small difference is at about 3 Hz, where the *Cb* array shows a weak secondary peak (Fig. 7a). The H/V amplitudes show values below 1 between 1.5 and 6 Hz (Fig. 7a), where the vertical component is more energetic than the horizontal

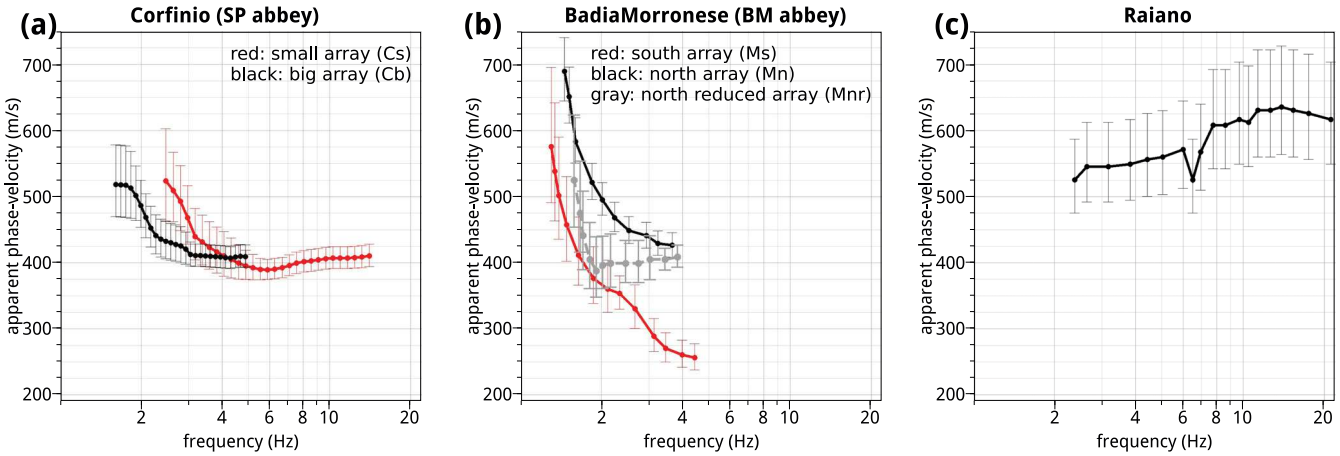

Figure 6. Experimental dispersion curves measured by 2-D arrays at (a) *SP,* (b) *BM* and (c) at *Raiano* site. We also computed a dispersion curve at *BM* that does not include some stations from the northern array that show inconsistent H/V curves to obtain the grey dispersion curve (*Mnr* in panel b).

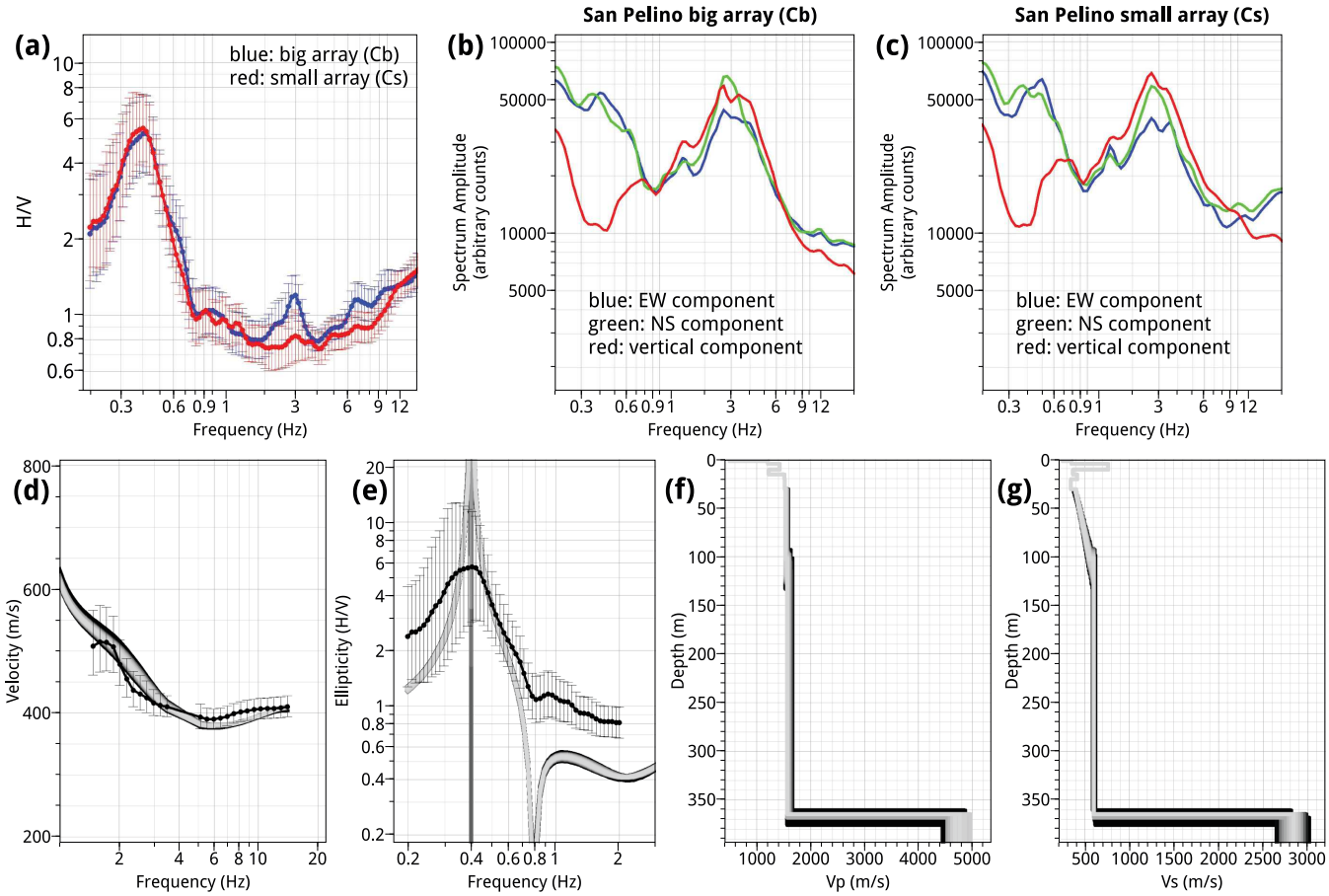

Figure 7. Results of the 2-D array experiment at the *SP* site. (a) H/V curves obtained by averaging the H/V curves of the stations within the two arrays (*Cs* and *Cb*). The red and blue curves refer to the smallest (*Cs*) and biggest (*Cb)* array, respectively. (b) Average FAS of the EW, NS and vertical components of the *Cb* array. (c) Average FAS of the three components of the *Cs* array. (d) Comparison between the experimental and best-fitting Rayleigh dispersion models (fundamental mode). The black curve with error bars is the combined dispersion curve of the two arrays *Cs* and *Cb.* (e) Comparison between the experimental H/V curve and best-fitting Rayleigh ellipticity models for the fundamental mode. The black curve with error bars is the mean H/V curve that was obtained by averaging the two experimental H/V curves shown in (a). The ellipticity peak of the Rayleigh waves is assumed to be at f_0 (∼0.4 Hz) during the inversion, and is indicated as the vertical dark area. (f) Best-fitting *Vp* models. (g) Best-fitting *Vs* models.

one (Figs 7b and c). Moreover, the correspondence of the H/V and spectra between *Cb* and *Cs* suggests the validity of a homogeneous model near the *SP* abbey, as shown in the geological model of Fig. 5. The main geological complexity at *SP* is likely related to a velocity reversal within the uppermost 20 m as indicated by the geological and down-hole surveys.

The *Cb* and *Cs* arrays show phase-velocities that overlap starting from 4 Hz (see Fig. 6a). The discrepancies at lower frequencies can

be explained in terms of the resolution capability, which is related to the array geometry. Below 4 Hz, *Cb* gives a better resolution than *Cs*. Therefore, we combine the two curves selecting below and above 4 Hz on the *Cb* and *Cs* dispersion curves, respectively. The resulting dispersion and H/V curves that were used in the joint inversion of the *SP* site are shown in black in Figs 7(d) and (e), whereas the models that were obtained during the inversion process are represented in a grey scale depending on the misfit values (Wathelet 2008). During the inversion at the *SP* site, the velocity of the uppermost 30 m was constrained by following the down-hole profile (shown in Fig. 5). This choice is motivated by the low resolution of our array (linked to its geometry; Renalier & Endrun 2009) for wavelengths (λ) lower than 30–40 m. The velocity models, which were derived from the inversion by using these constraints in the uppermost 30 m, are shown in Fig. 7(f) (*Vp*) and 7g (*Vs*). We achieved a good agreement between the inverted models and experimental curves by considering (i) the uppermost part of the lacustrine layer following a linear *Vs*-depth function and (ii) the deepest lacustrine deposits with an almost constant *Vs* of 600–650 m s^{-1} (Fig. 7g). The bedrock depth, which is mainly constrained to 0.4 Hz by the f_0, was found at approximately 370 m, which agrees well with independent gravimetric data (350–400 m; see the geologic section in Fig. 5).

The *Raiano* site is about 2 km SW of the *SP* abbey. A 2-D array of 12 seismic stations and with a maximum aperture of 170 m was additionally deployed to investigate the variation along the *SP-Raiano* direction in the *BB′* section (see Fig. 2). The H/V curves at the *Raiano* array (Fig. 8a) are quite similar to those observed at *SP* (Fig. 7a) but with a strongest peak, and the f_0 of 0.39 Hz indicates a deep seismic basement (probably at a depth larger than 350 m). The dispersion curve at *Raiano* shows the typical shape of a not normally dispersive site (Fig. 6c), with larger velocities than those measured at *SP* (Fig. 6a). The *Vs* models at *Raiano* (Fig. 8f), which were obtained from the surface wave inversion, indicate a stiff layer that is likely composed of gravels that has a bottom depth between 25 and 50 m, and overlies a lacustrine layer with a mostly constant *Vs* (600–650 m s^{-1}). The seismic bedrock is found at a depth of 400–500 m (Fig. 8f).

4.2 Fault-controlled basin margin: *Badia Morronese abbey*

4.2.1 Subsurface geological model

The second key site is the *BM* abbey (Fig. 2), which is located in the eastern part of the Sulmona Basin in the hanging wall of the *MMFS*, at a distance of ∼800 m from the trace of its western segment (Fig. 9). Due to the continuous activity of the *MMFS*, the *Mt. Morrone* slope was repeatedly rejuvenated during the Quaternary, alimenting the sedimentation of coarse-grained slope-derived debris and alluvial fans. Alluvial fan gravels prograded within the basin

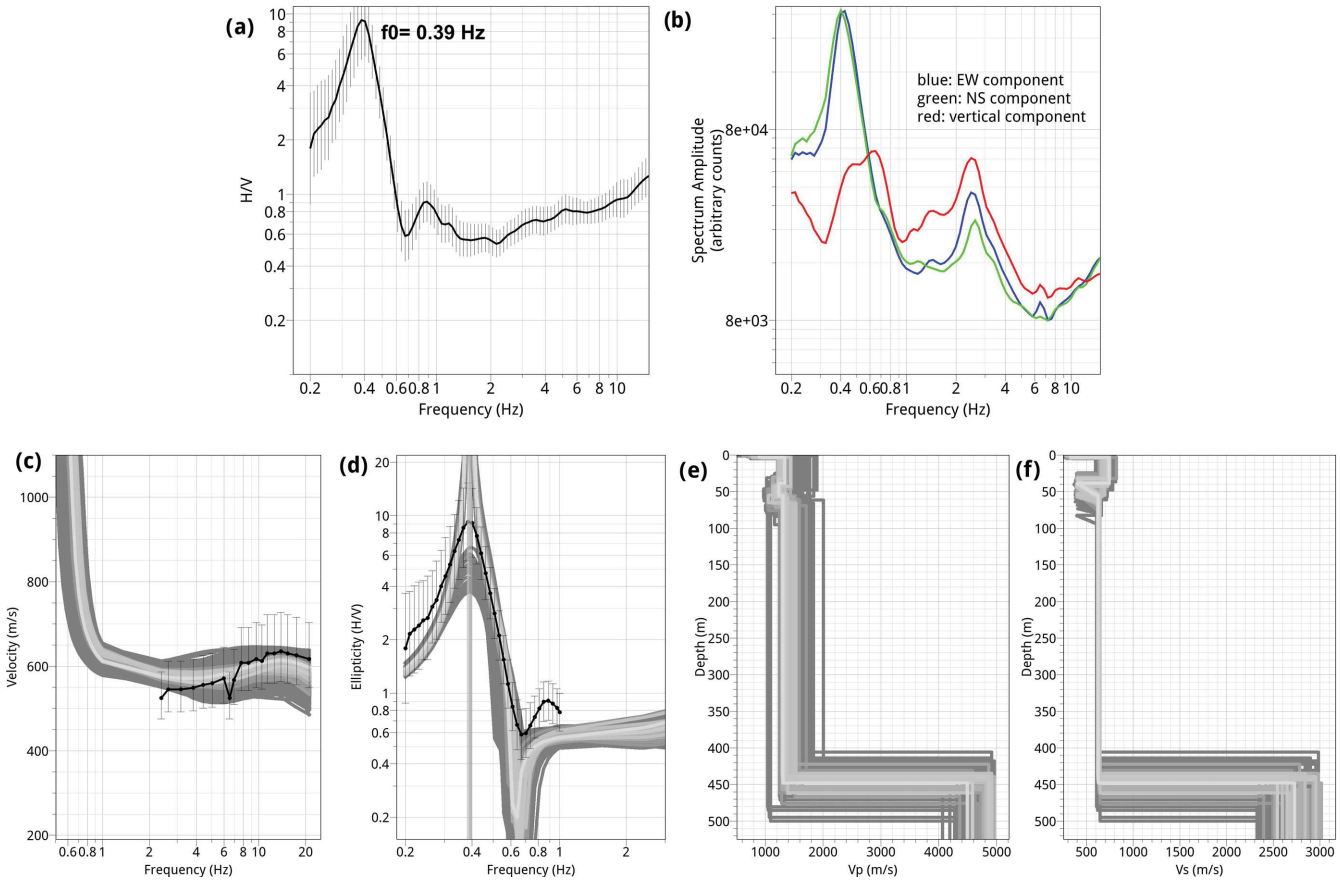

Figure 8. Results of the 2-D array experiment at the *Raiano* site. (a) H/V curve that was obtained by averaging the H/V curves of the stations within the array. (b) Average FAS of the EW, NS and vertical components. (c) Comparison between the experimental and best-fitting Rayleigh dispersion models (fundamental mode). The black curve with error bars is the measured dispersion curve. (d) Comparison between the experimental H/V curve and best-fitting Rayleigh ellipticity models. The black curve with error bars is the average H/V curve of the array. The ellipticity peak of the Rayleigh waves is assumed to be at f_0 (∼0.4 Hz) during the inversion, and is indicated as the vertical dark area. (e) Best-fitting *Vp* models. (f) Best-fitting *Vs* models.

due to the sediment supply, particularly during cold climatic periods, and interfingered with or covered fine-grained lacustrine sediments (clay and silt). Section A-A′-A″ in Fig. 9 illustrates a reconstruction of the subsurface geology up to the bedrock based on gravimetric data (Miccadei *et al.* 1998), passive experiments (this work, see next section), and data from a commercial seismic line. This last source, despite its poor quality in the shallowest part, provides insights on the thickness of the continental sedimentary cover (line IT-90-201, available at http://unmig.sviluppoeconomico.gov.it/). Beneath *BM*, the top of the bedrock is located at a depth of 250 ± 50 m, and deepens slightly westwards. In our opinion, it is not possible to discriminate wheter the bedrock is formed by pre-Quaternary carbonate

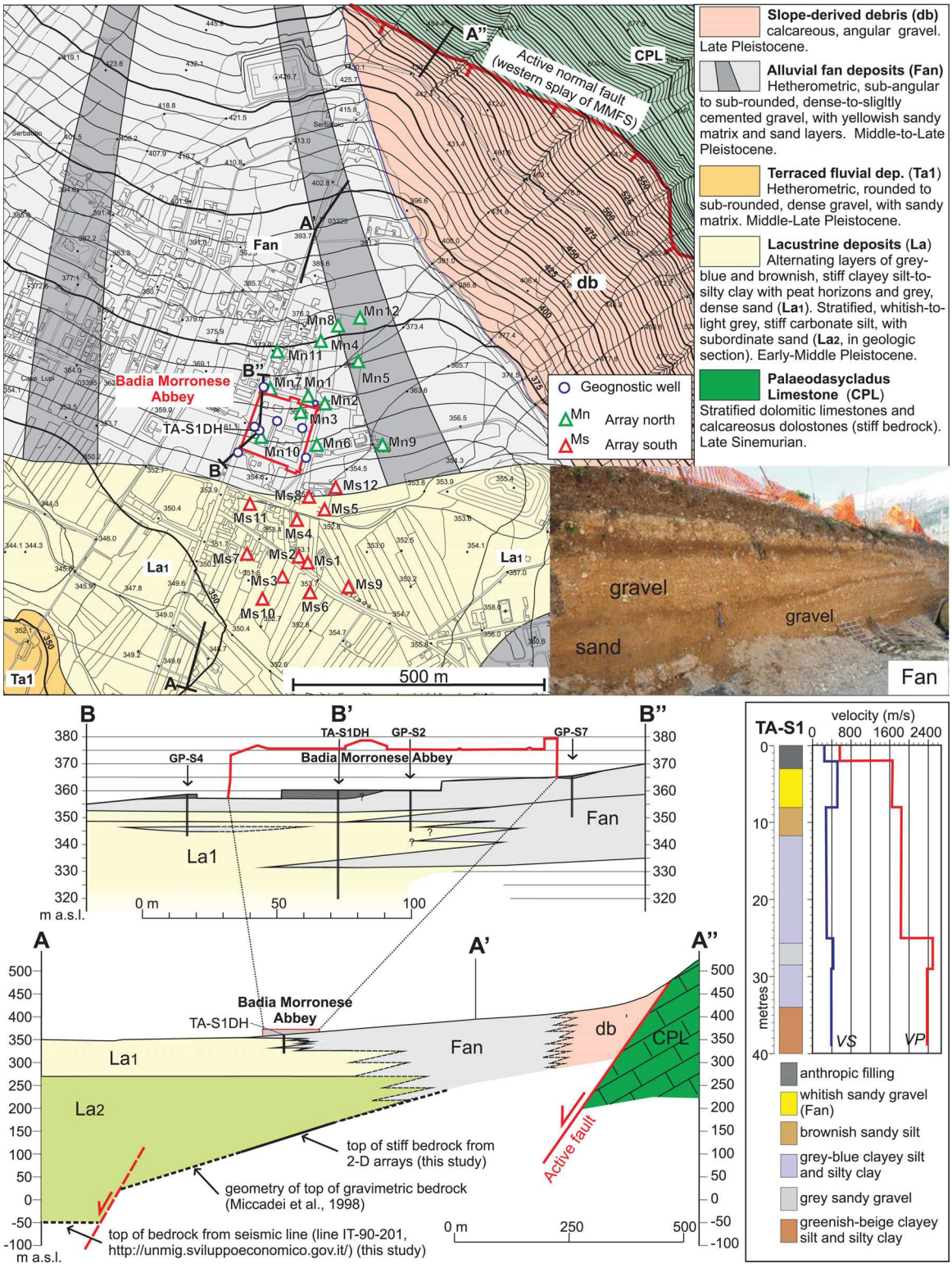

Figure 9. Geological map of the area surrounding the *Badia Morronese* abbey (location in Fig. 2). The picture shows the field view of the Fan unit. The stratigraphy is also shown, with the *Vp* and *Vs* down-hole profiles from a pre-existing 40-m-deep geognostic well (from Tatoni 2011).

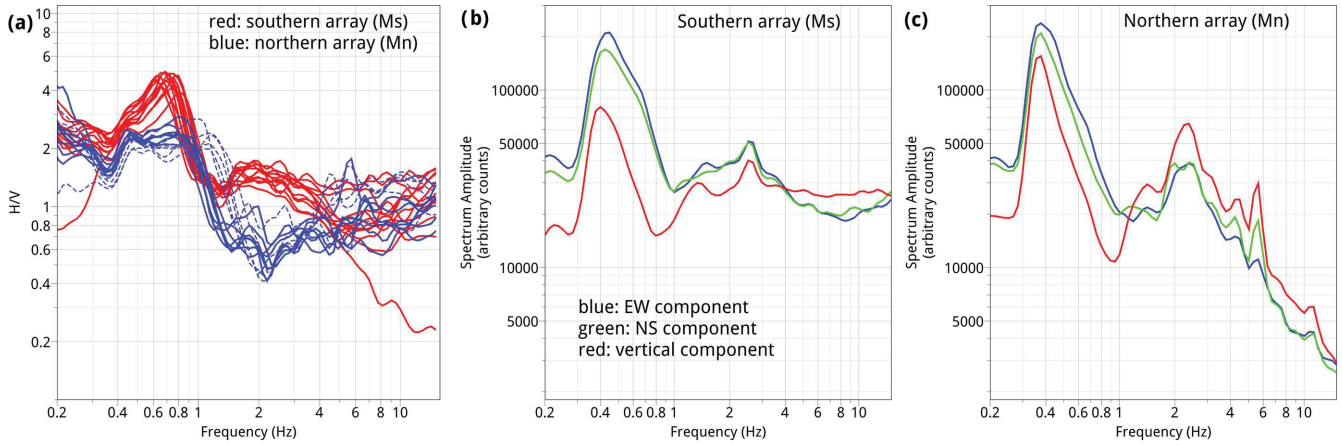

Figure 10. Ambient noise analysis at the *BM* site. (a) Average H/V curves. The red and blue curves refer to the southern and northern array, respectively. The dashed H/V curves refer to the sites M*n04*, M*n05*, M*n08*, M*n09* and M*n12* from the northern array (not considered in the *Mnr* array; see text). (b) Average FAS of the three components of ground motion for the southern array (*Ms*). (c) Average FAS of the three components of ground-motion for the northern array (*Mn*).

rocks or by old, stiff Quaternary deposits (e.g. stiff Lower-Middle Pleistocene breccia). For the purpose of evaluating the site response, this difference does not seem to have a particular relevance. Towards the east, the basin is bounded by the normal fault, which is clearly visible in outcrops and in the IT-90-201 seismic line. In the hanging wall of the main fault, a synthetic splay can be drawn on the seismic line. In our interpretation, the maximum thickness (400–450 m) of the continental infilling is in the hanging wall of the synthetic splay.

The shallow subsurface geology is also illustrated in section B-B′-B″ in Fig. 9, and is constrained by 15–40-m-deep geognostic wells (professional reports by Geoplanning 1999 and Tatoni 2011; made available by the Italian Ministry of Cultural Heritage – MiBAC, Ministero per i Beni e le Attività Culturali). A body of dense-to-medium dense gravels and sandy gravels that thins progressively westward exists beneath *BM*. The gravels form the distal part of the large alluvial fan that is observed at the surface in the hanging wall of the *MMFS* (Fig. 9). The fan-gravels overlay finer sediments that consists of firm sandy silt, clayey silt and silty clay. Interlayers of gravels are present at different depths within the lacustrine sediments. The pelitic sediments that were drilled by the deepest geognostic well (TA-S1 well in Fig. 9) can be tentatively correlated with the Middle Pleistocene *La1* unit in the *Corfinio* area. The deepest lacustrine deposits are not constrained by either borehole or field data, but can be reasonably considered to be similar to the Lower-Middle Pleistocene, stratified, whitish-to-light grey, stiff carbonate silt that is observed in outcrops in the *Corfinio* area (*La2* unit). The boundary between *La1* and *La2* occurs at a depth of ∼80 m (Fig. 9), corresponding to a significant step in our velocity profile (see next section). A downhole profile is also available for the 40 m-deep borehole that was drilled at *BM* (TA-S1 in Fig. 9). The sandy gravels have a *Vs* of ∼510 m s^{-1}, and a velocity inversion occurs at the transition with the underlying fine-grained sediments (*Vs* decreases from 510 to 290 m s^{-1}); then, the *Vs* remains within 290–400 m s^{-1} up to depths of ∼40 m, with local increases due to gravel interlayers. The *Vs* is approximately 250 m s^{-1} where the upper gravel layer is very thin and pelitic sediments are close to the ground surface (Tatoni 2011).

4.2.2 2-D array: results

The two adjacent arrays, which were deployed with similar geometries and maximum apertures (about 300 m) north and south of the *BM* abbey, provide evidence of an abrupt change in the near-surface geology, which is related to the presence of alluvial fan gravels.

The H/V and spectral curves at *BM* show strong differences amongst close stations (Fig. 10). The stations from the southern array (*Ms*) show a clear H/V peak at 0.7 Hz (Fig. 10a). The stations from the northern array (*Mn*) show plateau-shaped H/V curves between 0.4 and 1.3 Hz (with an average amplitude level of 2), making the discrimination of a resonance frequency difficult (Fig. 10a). Moreover, the *Mn* stations show H/V ratios with amplitudes less than 1 starting from 1 Hz, which is due to the greater energy content of the vertical component (Fig. 10c) and is likely related to the effect of the *Vs* reversal in the near-surface geology (Castellaro & Mulargia 2009b). The FAS of the *Mn* array shows also a strong energetic decay starting from 4 Hz for all three components of ground motion (Fig. 10c). Some small discrepancies in the H/V curves are also observed for some stations within the northern array; indeed, the stations in the NE sector of the *Mn* layout array (M*n04*, M*n05*, M*n08*, M*n09* and M*n12;* see Fig. 9 for locations) show larger frequency band of amplification in the plateau shape (up to 1.4 Hz; the H/V ratios of these stations are shown as dashed curves in Fig. 10a).

The dispersion curves of the *Mn* and *Ms* arrays also show differences. The southern array at *BM* gives apparent velocities that are lower than those from the northern array (Fig. 6b). Based on the similarity among the H/V curves, we decided to invert i) the dispersion curve that was estimated at the southern array, and ii) the dispersion curve that was recomputed at the northern array excluding the M*n04*, M*n05*, M*n08*, M*n09* and M*n12* sites (this new reduced array is named *Mnr*). The dispersion curve of the *Mnr* array (grey curve in Fig. 6b) shows still larger velocities than those from the southern *Ms* array; this is true over the entire frequency band of analysis.

The joint inversion of the velocity dispersion and mean H/V curve is shown in Fig. 11 for both the *Ms* and *Mnr* arrays. The velocity models are consistent with the geological observations, with an upper 20–40-m-thick high-velocity layer that is correlated with the fan gravels that crop out north of the *BM* abbey. A velocity inversion exists below the high-velocity layer, corresponding to the transition to fine-grained lacustrine sediments (Figs 11g and h). This shallow high-velocity layer is not present south of the abbey, whereas the fan gravels are absent, and the *Vs* models show a normally dispersive profile at the *Ms* array (Figs 11c and d).

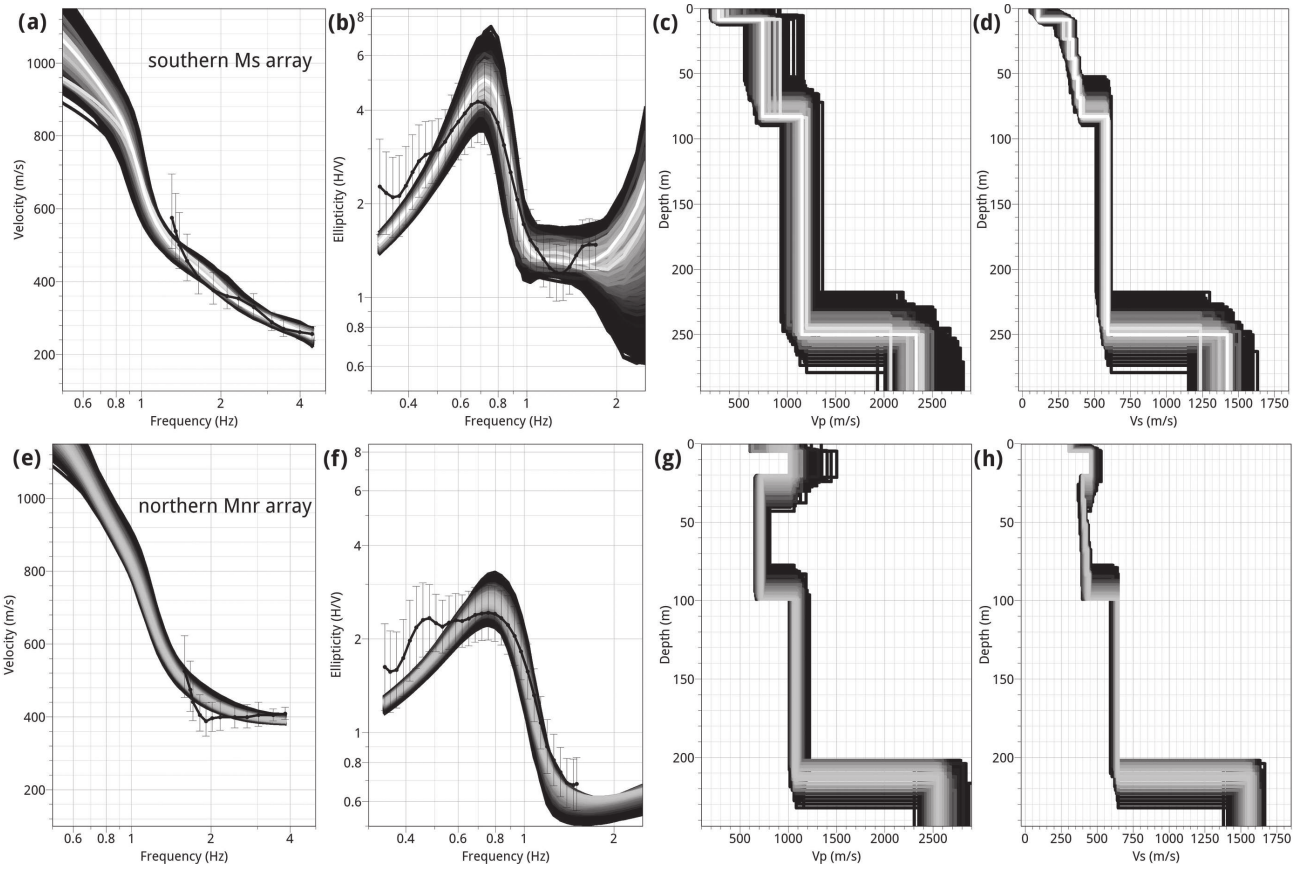

Figure 11. *BM site.* Inversion results for the southern *Ms* array (top panel) and northern *Mnr* array (bottom panel). The stations M*n04*, M*n05*, M*n08*, M*n09* and M*n12* from the northern array were not considered (see text). (a) and (e) Comparison between the experimental and best-fitting Rayleigh dispersion curves (fundamental mode). The black curve with error bars is the measured dispersion curve. (b) and (f) Comparison between the H/V and best-fitting Rayleigh ellipticity models (fundamental mode). The black curve was obtained by averaging the H/V curves of each array. (c) and (g) Best-fitting *Vp* models. (d) and (h) Best-fitting *Vs* models.

From the inversion of both arrays, the lacustrine deposits (i) show a *Vs*-depth function that follows a linear law up to a maximum depth of 100 m, (ii) passing downward to a second layer with a constant *Vs* of 600 m s^{-1}. Note that for the northern *Mnr* array, the ellipticity models only partially fit the plateau shape of the observed H/V curve (Fig. 11f).

5 1-D AND 2-D MODELLING AT SITES WITH VELOCITY INVERSIONS

5.1 1-D modelling

The 1-D numerical simulations focus on investigating the seismic response at the two key sites of *SP* and *BM*, where the *Vs* profile is characterized by a velocity inversion within the soil profile.

We performed 1-D linear equivalent site response analyses (EERA code; Bardet *et al.* 2000) by taking into account real earthquake records from a similar seismotectonic context. The models that were used in the 1-D computation were reconstructed in the previous sections (see Sections 4.1 an 4.2). The *Vs* profiles at the two sites (Fig. 12) were taken from the best models that were provided by the inversion of surfaces waves.

For *BM*, we performed two numerical analyses to account for the different stratigraphy that was observed north and south of the abbey. For the input motion, we adopted two accelerograms (Fig. 13) that were recorded during the April 6, 2009 L'Aquila earthquake (M_w = 6.3; Pondrelli *et al.* 2006 and 2010) at two stations (AQU and MTR) belonging to the National Seismic Network and Italian strong-motion network (Gorini *et al.* 2010), and are classified as soil class A (NTC08). These two accelerograms were recorded at an epicentral distance of 6 and 23 km (Zambonelli *et al.* 2011), therefore representing near (AQU) and far (MTR) field strong motions. Given the purpose of this study, we did not scale the peak ground acceleration (PGA) to the value prescribed by national seismic codes. However, this reference value in the Sulmona Basin is of the same order as the PGA that was recorded at AQU (about 0.3 g when a return period of 475 yr is considered; see Fig. 13).

The non-linear and dissipative properties of the soils, considered for the numerical analyses, are summarized in the supplementary material (Fig. S1 and Table S1) in terms of the normalized shear modulus (G/Gmax) and damping ratio (D) versus the variation in the shear strain. The characteristics of silty clay/clayey silt (b in Fig. S1) were derived from a cyclic, dynamic laboratory test (resonant column) on an undisturbed borehole sample. The non-linear properties of gravel (a in Figs 12 and S1) were assigned based on literature curves that were derived in the framework of the Italian seismic microzonation project (MS Working Group 2008). The curves of silty sand and white lacustrine silt (c and d in Figs 12 and S1) were taken from the MS-AQ Working Group (2010). These curves were derived from cyclic, dynamic laboratory tests on borehole samples from sites with comparable soil characteristics close to our study areas.

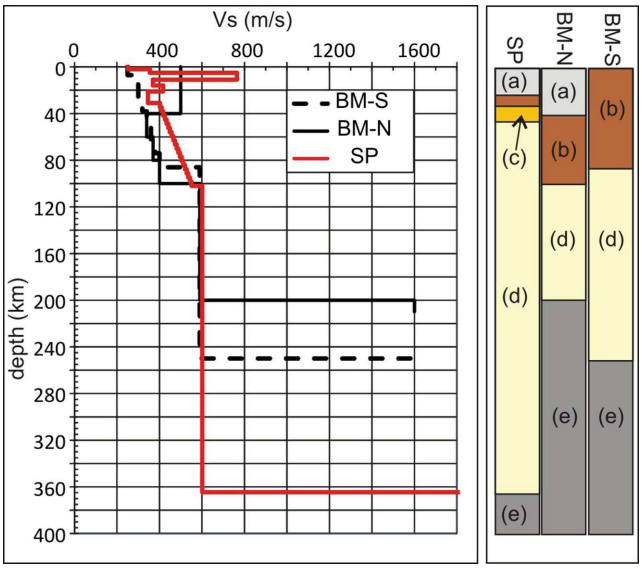

Figure 12. Velocity models that were used in the 1-D numerical simulation. The stratigraphic columns are shown on the right: the gravel layer is marked by (a), the silty-clay/clayey-silt is marked by (b), the silty sand is marked by (c), the white lacustrine silt is marked by (d), and the bedrock is marked by (e).

Fig. 13 shows the different behaviours among the analysed sites in terms of their response spectra. The output response spectra at *SP* do not show pronounced peaks below 0.2 s (above 5 Hz) even if the input ground motion (AQU and MTR) presents clear narrow peaks at those frequencies. On the contrary, southern *BM* reveals significant amplification, also at high frequency, when compared to the response of the northern *BM* and *SP* sites. An interesting bump within 2–3 s is evident at *SP*, which is probably related to the resonance of the deep basin (Fig. 13).

To better quantify the differences among the key sites, we smoothed the resulting response spectra following the criteria indicated by the MS Working Group (2008). If we consider AQU recordings and the *Badia Morronese* site (Fig. 14), souther *BM* has an average spectral acceleration for both components of approximately 0.9 g within periods of 0.3–1.2 s, which are higher than those in northern *BM* (0.82 g within 0.25–0.9 s). A similar trend is observed when we consider the MTR input motions: the southern *BM* area shows significant amplifications over a wide frequency range, while the northern *BM* area shows the lowest ground motion values (Fig. 14). This low magnification at northern *BM* with respect to southern *BM* is related to the presence of the stiff superficial layer. The response spectra of *SP* seem more dependent on the input motion. When computed with the NS component of AQU and MTR, *SP* shows a spectral acceleration between those of *BMs* and *BMn*. When computed with the EW component of AQU and MTR, *SP* has a spectral plateau level that is slight higher and lower than those for *BMs* and *BMn*, respectively.

5.2 2-D modelling

Our investigations show that the near-surface geology of the Sulmona Basin is often characterized by a rigid uppermost layer, the thickness of which is on the order of a few tens of meters. The role played by the velocity inversion that is associated with a stiff layer, on both the H/V ratios and surface-wave dispersion curves, is now investigated by 2-D numerical modelling. Modelling H/V curves in the presence of an uppermost stiff and thin layer has been already performed by Castellaro & Mulargia (2009b) by means of 1-D computations of surface-waves ellipticity (based on the code of Herrmann & Ammon 2002). By computing forward 1-D models of theoretical ellipticity and dispersion curves, reproducing similar results to the ones found by Castellaro & Mulargia (2009b) is straightforward. Increasing the *Vs* or the thickness of the uppermost stiff layer (Fig. 15) leads to ellipticity curves with amplitudes below 1, and the dispersion curves show a more complex shape with inflection branches in a certain frequency band. Our improvement with respect to the previous works is in the use of a 2-D model to investigate the effect of a superficial stiff layer in terms of both H/V and dispersion curves.

For the 2-D numerical computation, we used the spectral element method (SEM, as implemented in the *specfem2d* code, http://geodynamics.org/cig/software/specfem2d/; Komatitsch & Vilotte 1998; Chaljub *et al.* 2007) to propagate surface waves in simple layered models. SEM is one of the most effective strategies to address seismic wave modelling (Komatitsch & Tromp 2002; Stupazzini 2004; Chaljub 2006; Lee *et al.* 2009; Smerzini *et al.* 2011; Cupillard *et al.* 2012); its peculiarity consists in the combined use of high-order Legendre polynomials and the Gauss–Lobatto–Legendre (GLL) quadrature rule in evaluating integrals within the weak (or variational) formulation of motion equation (Fichtner 2011).

Specifically, we simulated in-plane waves (P-SV) by considering two simple models: without and with the presence of a stiff superficial layer (Fig. 16). The first model (*soft model* hereafter) was simply a 50-m-thick soft layer with a *Vs* of 200 m s^{-1}, overlying a basement with a *Vs* of 800 m s^{-1}. The resonant frequency of this model is 1 Hz as given by the 1-D quarter wavelength approximation ($f_0 = Vs/4H$). The second model (*stiff model* hereafter) consisted of an uppermost stiff layer (15 m thick, $Vs = 800$ m s^{-1}) overlaying a softer layer (35 m thick, $Vs = 200$ m s^{-1}). The half-space interface was located at a depth of 50 m, and the *Vs* of the bedrock was fixed to 800 m s^{-1} (Fig. 16). These simple models do not consider the deep geometry of the Sulmona plain and do not attempt to reproduce any real geological section. The used models intend to investigate the influence of a stiff uppermost layer on the ground motion by using thickness and velocity contrasts that are comparable to those observed in real situations. A parametric analysis with many models, which considers the signatures of different impedance contrasts on H/V and dispersion curves, is beyond the scope of this paper. The *Vp* velocities and *Q* factors are indicated in Fig. 16; the *Vp* values were selected according to Castellaro & Mulargia (2009b), and the *Q* values were selected following the rule of thumb of velocities divided by 10. The density of the model was fixed to 2 g cm^{-3}. The total dimension of the computational domain was of 2000 and 900 m (*x*- and *z*-directions, respectively) for both models. The receivers, in number of 300, were located along the topographic surface on the *x* axis (progressively from 10 to 1990 m), with a regular spacing of about 6.6 m between adjacent receivers. The left, right and bottom sides of the models were absorbing boundaries that used perfectly matched layers (PML) spectral elements (Fichtner 2011). The mesh of the P–SV models was built by the internal mesher tool that was available in *specfem2d* and used rectangular reference elements. A zoom of the mesh is illustrated in Fig. 16. Assuming a maximum frequency of investigation (f_{max}) of 10 Hz and considering that *Vs* in the soft layer is 200 m s^{-1}, the minimum wavelength is 20 m ($\lambda_{min} = V_{min}/f_{max}$). The mesh respects the stability condition on the size (Fichtner 2011), guaranteeing at least four grid spacings per λ_{min}. The time step was fixed to 1×10^{-4} s, and the time length of the output synthetics was set to 16 s.

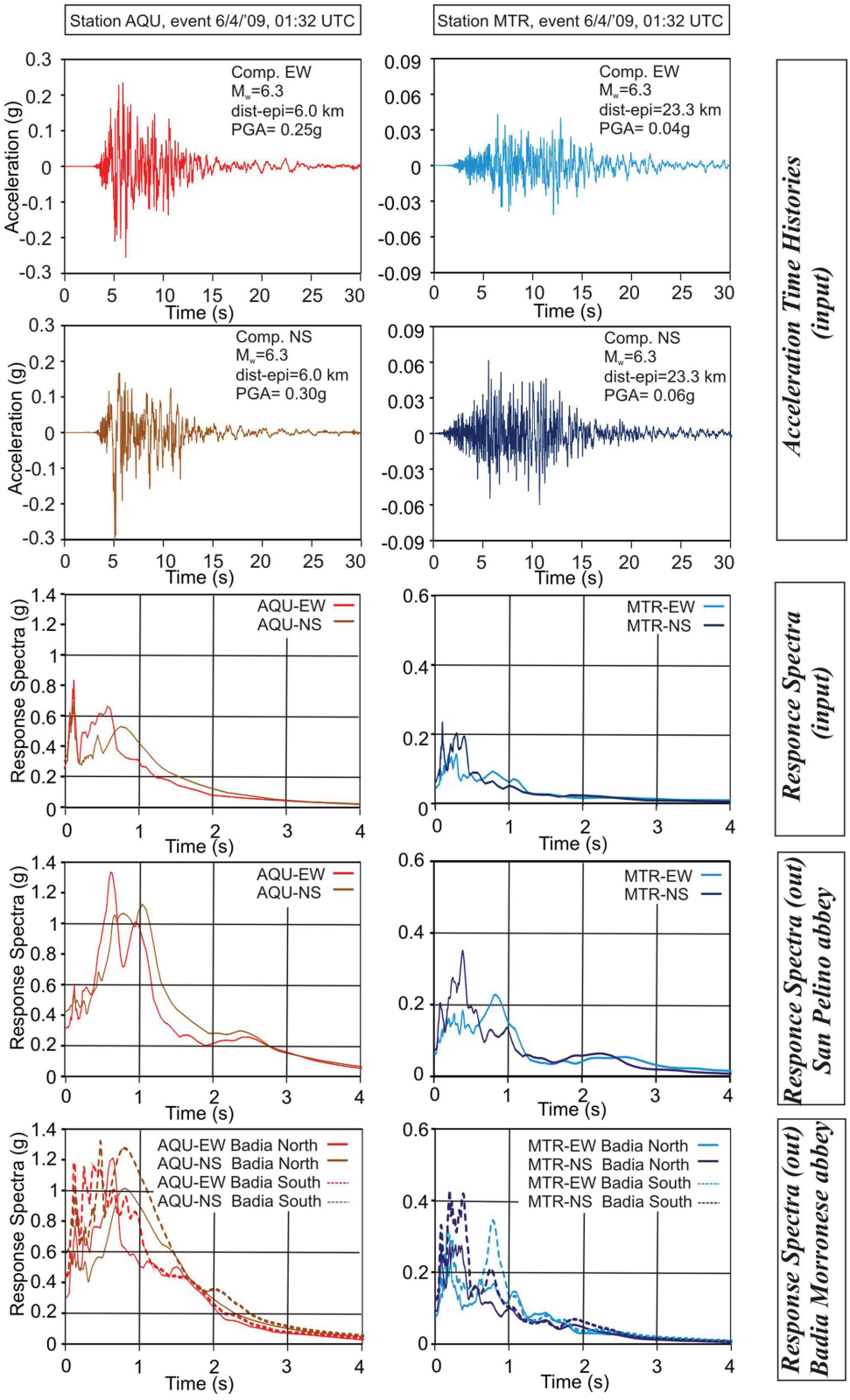

Figure 13. 1-D numerical analyses at the *San Pelino* (*SP*) and *Badia Morronese* (*BM*) sites including the time histories and input- and output-response spectra.

To model laterally propagating surface waves, a Dirac source was initially located in the soft layer near the left boundary of the model (Fig. S2). Under this condition, the interferences between directed and diffracted waves that are trapped in the soft layer generate surface waves, which propagate from the left to the right side of the model (Fig. S2). This is consistent with the fact that the noise wavefield is supposed to be dominated by surface waves, and is generally modelled as a superposition of punctual sources located near the surface (e.g. Bonnefoy-Claudet *et al.* 2004; Lunedei & Albarello 2010).

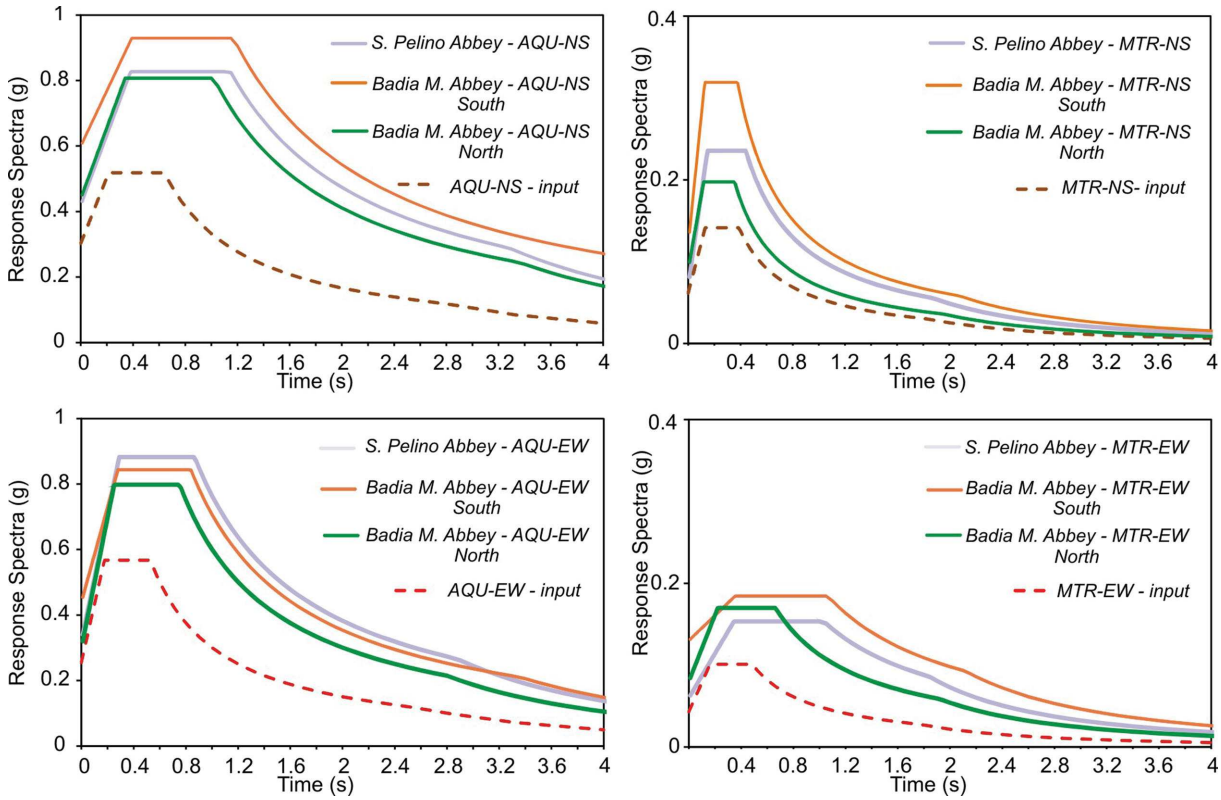

Figure 14. Comparison of the smoothed spectral accelerations at *SP* and *BM* sites. The output response spectra in Fig. 13 were smoothed following the criteria suggested by the MS Working Group 2008.

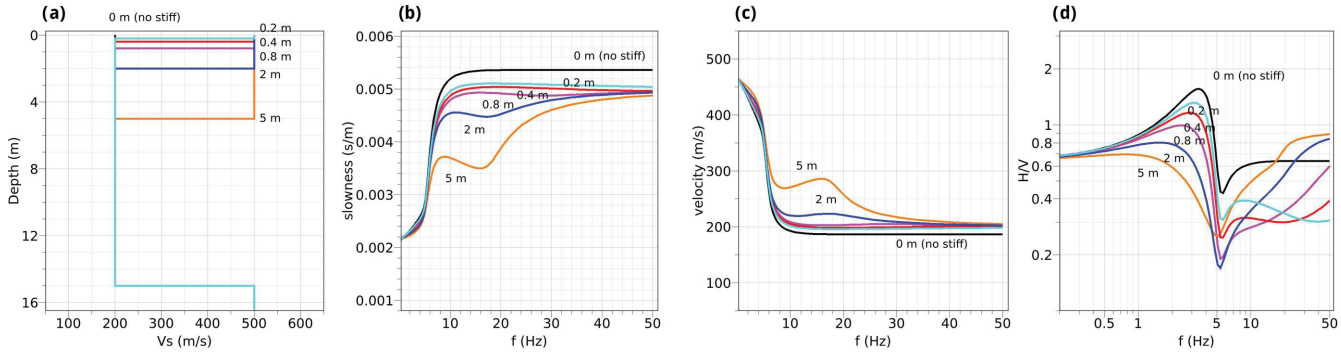

Figure 15. Results from forward 1-D computations of the Rayleigh fundamental mode. (a) Subsoil models (following some *Vs* profiles from Castellaro & Mulargia 2009b). The thickness of the stiff shallow layer varies: 0 m (no stiff layer), 0.2, 0.4, 0.8, 2 and 5 m. Each colour refers to one specific model. (b) Dispersion curves in slowness; (c) The same as (b) but in velocity; (d) Ellipticity curves. The forward calculation is done by using the *geopsy* tool (www.geopsy.org).

An example of a displacement output file at a generic receiver is shown in Fig. S3, with the whole stack of the synthetics shown in Fig. S4 in the supplementary material. For both models, the vertical components exhibit a clear propagating late phase at about 2 Hz, and larger amplitudes compared to those for the horizontal components (Fig. S3).

The FAS of a group of receivers shows the spectral behaviours of the x and z components. When the stiff uppermost layer is not present (Fig. 17a), the *x* component is more energetic than the z component around the resonance frequency ($f_0 = 1$ Hz), but the vertical component has larger amplitudes starting from 1.25 to 1.5 Hz, with a clear spectral peak at 1.8 Hz. When the uppermost stiff layer is present (Fig. 17b), the two components of the motion are well separated up to 5 Hz. Furthermore, the vertical component has larger amplitudes with respect to the horizontal component in the whole frequency band except at about 1 Hz, where the horizontal components show the same amplitude level as the vertical component (Fig. 17b).

For the *soft model*, the H/V curves that were computed on synthetics (Fig. 17c) sufficiently match the f_0 at 1 Hz. A good fit at 1 Hz is also achieved between the H/V curves and the SH theoretical transfer function of the 1-D layered model, and this fit agrees with the numerical results of Bonnefoy-Claudet (2004) and Bonnefoy-Claudet *et al.* (2006). The f_0 fit in terms of the frequency value

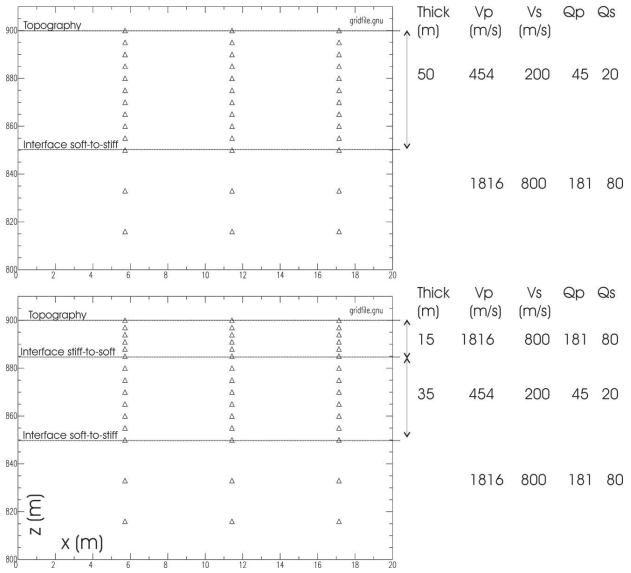

Figure 16. Zoom of the grid points that were used for the SEM 2-D simulation. (Top) *Soft model*. (Bottom) *Stiff model*. The right table shows the thickness, velocity and quality factor values. The size in the mesh of the reference four-sided element is 5.7 and 17 m (x and z) in the basement region; 5.7 and 5 m in the soft layer with has a Vs value of 200 m s^{-1}; and 5.7 and 3 m in the uppermost layer, which has a Vs value of 800 m s^{-1}.

between the theoretical ellipticity of Rayleigh waves and the H/V curve appears still acceptable, although a best match is obtained for the spectral trough at 1.8 Hz (corresponding to 2 f_0).

For the *stiff model*, the H/V curves that were computed on synthetics do not present more a strong spectral peak at 1 Hz (Fig. 17d). The H/V curves and the theoretical ellipticity show amplitudes essentially below 1, and a good fit between the H/V and ellipticity curve is clear from the trough at 1.8 Hz to higher frequencies. Interestingly, also the SH curve shows deamplification from 1.5 to 3 Hz and for frequencies higher than 5 Hz. However, the theoretical SH transfer function is not able to match the H/V curves.

To investigate the effect of the uppermost stiff layer also on surface wave dispersion curves, a linear f–k analysis has also been computed on the synthetic signals. The f–k analyses for both the *soft model* and *stiff model* show a predominant role of propagating Rayleigh waves on both the x and z components. The theoretical Rayleigh dispersion curves that were computed by the 1-D forward modelling are also reported in Fig. 18 (white curves). For the *soft model* (Fig. 18b), the f–k estimator adequately discriminates the fundamental and first higher Rayleigh modes in all frequency bands and for both components. No significant jumps between modes are observed (Fig. 18b). For the *stiff model* (Fig. 18a), the f–k analysis returns dispersion curves with the typical shapes of a not normally dispersive site (i.e. slowness does not always increase with frequency). The theoretical fundamental mode of the Rayleigh

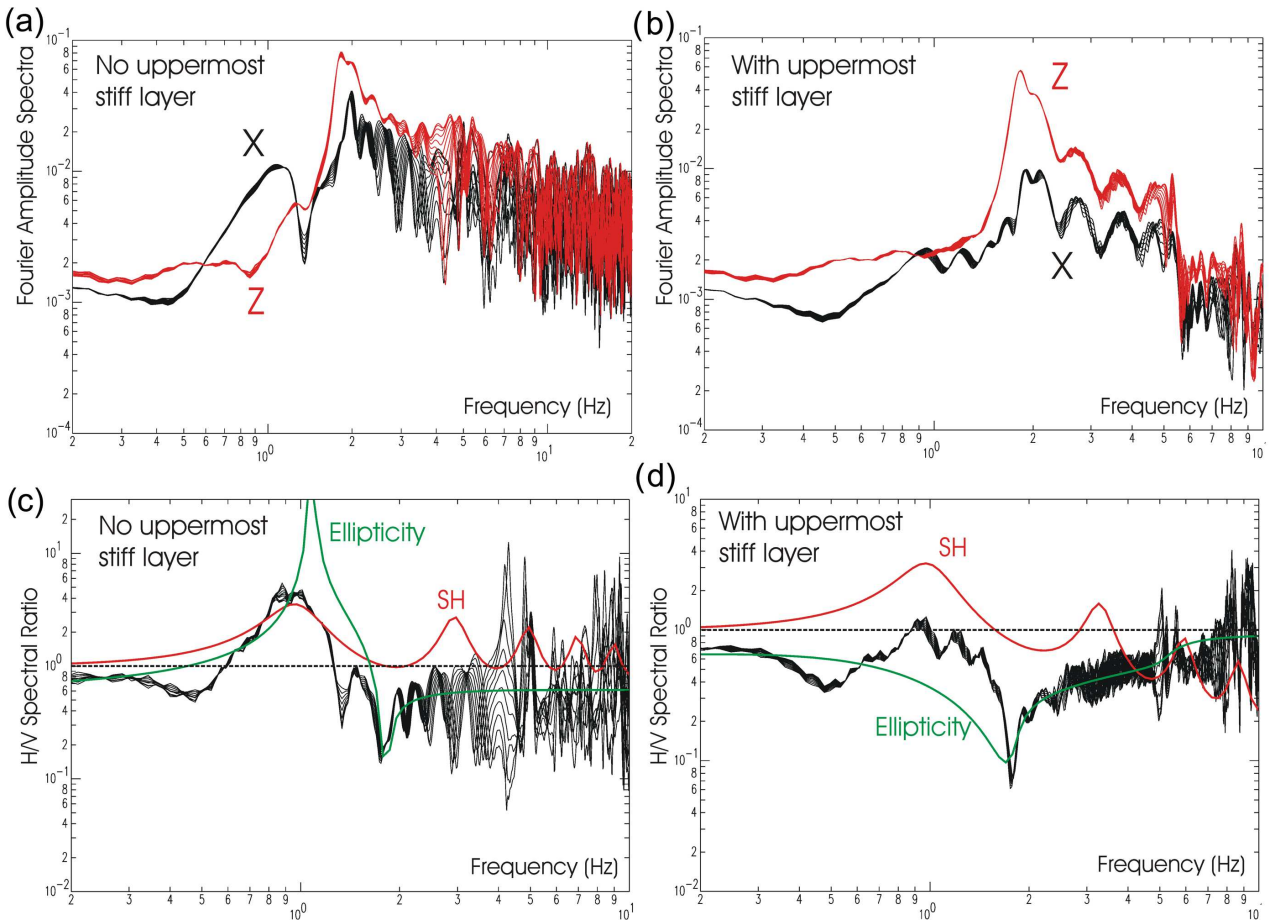

Figure 17. Results of the 2-D numerical modelling. The top panel shows the FAS of the *soft model* (a) and of the *stiff model* (b). The FASs of the vertical (z) and horizontal (x) components are shown in red and black, respectively. The FAS refer to a group of receivers from 798 to 858 m in the x direction. The bottom panel shows the corresponding H/V black curves that were computed for the *soft model* (c) and the *stiff model* (d). The theoretical ellipticity of the fundamental mode of the Rayleigh waves, and the theoretical SH transfer function are also shown (green and red curves, respectively).

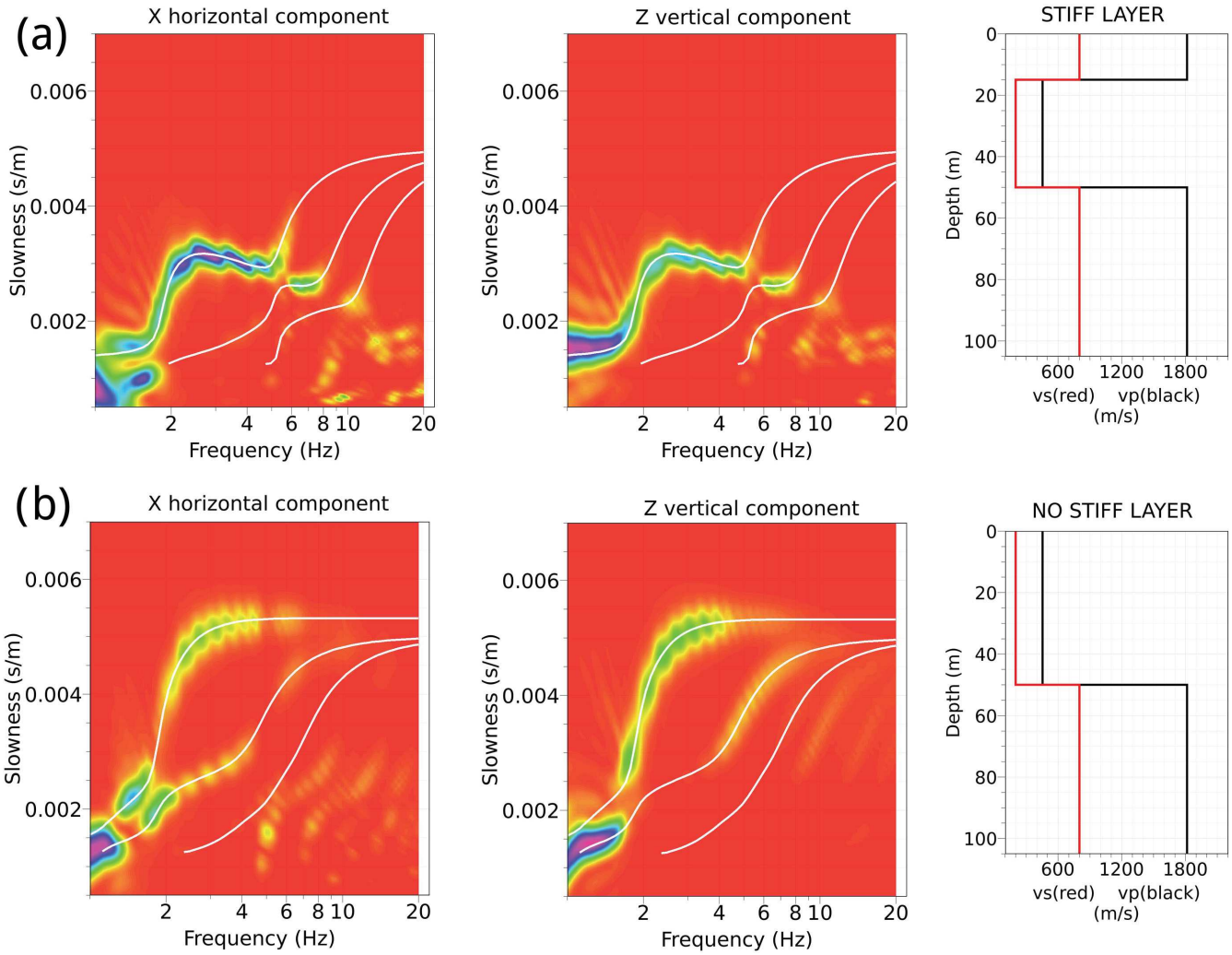

Figure 18. *F–K* analyses on the synthetic signals for the *stiff model* (a) and the *soft model* (b). The left-hand panel shows the comparison between the theoretical and calculated dispersion curves for the horizontal radial component. The central panel shows the comparison between the theoretical and calculated dispersion curves for the vertical component. The theoretical 1-D forward dispersion curves of the Rayleigh waves (first three modes) are shown in white. The right-hand panel shows the velocity models.

waves follows the actual *f–k* maxima for frequencies below 5 Hz. Jumps in the f-k maxima occurred due to higher modes; jumps from first to second- higher mode are observed for frequencies >5 Hz (Fig. 18a).

6 DISCUSSION AND CONCLUSIONS

The geological structure of the deep Sulmona Basin has been investigated by using H/V ratios and array noise methods based on surface-waves. We focused on two key sites in different positions within the basin, namely, the *Badia Morronese* (*BM*) *and San Pelino* (*SP*) areas. We mapped the variability of f_0 along two main basin-scale transects, pointing out an f_0 of 0.35–0.4 Hz in the deepest part of the basin. The H/V noise ratios were almost flat on the rock sites surrounding the basin, although weak amplification sometimes appeared at high frequencies (>3 Hz), which is likely related to fractured rocks close to the trace of the *MMFS*. The H/V method was used at these key sites in conjunction with 2-D small-aperture arrays, also to provide evidence of the heterogeneity in the near-surface geology near the edges of the basin. Independent data provided by near-surface surveys in specific points (e.g. MASW and down-hole surveys) refined the topmost shallow part of the inverted models, whereas our arrays generally could not depict variations over very thin layers within the profile. Similar experimental H/V curves were found by adjacent noise measurements around *SP*, which can be considered as a homogeneous layered model according to the geological information. In contrast, abrupt variations in the spectra and dispersion curves were observed over a relatively short distance in the *BM* area. The geological/geotechnical heterogeneities at *BM* are connected to alluvial fans that were alimented from the nearby mountain relief. An uppermost layer of relatively stiff gravels is predominant in the northern part of the *BM* area. This layer of gravels vanishes to the south of the abbey, where the H/V curves are characterized by a clear H/V peak, and the dispersion curves show lower apparent phase-velocities with respect to the northern area.

At the key sites, the surface-wave inversion provided a depth for the soft-to-bedrock interface that was consistent with the independent gravimetric data. The maximum depth of the bedrock from the inversion is on the order of 400–500 m near the *Corfinio* and *Raiano* villages ($f_0 = 0.4$ Hz), and 250–300 m near the *BM* abbey ($f_0 = 0.8$ Hz). Additionally, we found a velocity reversal for a maximum depth of 50 m in the near-surface geology at all the studied

sites. Interestingly, the national seismic code (NTC 2008) precludes a simplified approach to compute amplification factors when a velocity inversion is present in the local soil profile. We quantified the spectral amplification by means of 1-D modelling at the target sites, taking into account both the *Vs* profiles from the array analysis and the subsoil non-linearity from laboratory tests or the literature. We found that the spectral accelerations at the surface, with respect to the input motion, tend to be magnified in different frequency bands depending on the site. At *SP*, the spectral amplification is between 0.2 and 1 s. At *BM*, the spectral amplification in the southern area is shifted toward longer periods and is larger than the amplifications in the northern area. This difference is related to the presence of the superficial stiff layer in the northern area. When the seismic input is deep, the presence of a superficial stiff layer reduces the 1-D ground amplification (compared to a hypothetical site with an identical *Vs* profile except for the presence of this superficial stiff layer).

We also modelled the presence of a velocity inversion by means of a 2-D spectral element code. We used a very simple 2-D model generating travelling surface wave along the superficial layer. This agrees with the fact that the noise wavefield is assumed to be mostly related to surface waves. The results of basic 2-D numerical modelling in presence of the uppermost stiff layer agree with the observations. A velocity reversal within the near-surface profile (thickness of a few tens of meters in our case) significantly affects the spectra, the H/V shapes and the dispersion curves. The effect of an uppermost stiff layer on the H/V and dispersion curves is related to its thickness and to the velocity contrast caused by this stiff layer. Our 2-D modelling can be regarded as a type of 1.5-D model, allowing the lateral propagation of surface waves with a plane-parallel 1-D configuration. For a more realistic 2-D model, including a transition from thin to thick stiff covering and/or bedrock with a variable depth, the shapes of the H/V and dispersion curves are expected to show spatial variation along the 2-D model (as also indicated by Fig. 15). A further complexity with respect to 1-D behaviour could be related to diffracted/refracted waves within the wavefield in presence of an abrupt transition in the model, for example a subvertical interface between lacustrine soil and an alluvial fan.

In conclusion, dispersion curves that show a complex shape with inflection branches, in conjunction with H/V noise ratios with amplitudes below 1 in a certain frequency band, can provide insights regarding the presence of an uppermost stiff layer. This seems true when the noise wavefield is strongly dominated by surface waves, and array methods are a suitable tool to verify the goodness of this starting assumption.

A strategy that is based on ambient noise measurements, and supported by geological information, can be used to map the extension of the alluvial fan areas near the edges of intramontane basins. To this aim, the microzonation studies in the epicentral area following the damaging 2009 earthquake in central Italy (L'Aquila earthquake), which were based on extensive noise surveys coupled with subsurface geological and geophysical data, already provided favourable indications for mapping velocity inversions in alluvial fans and along mountain slopes (Boncio *et al.* 2011; Gallipoli *et al.* 2011).

ACKNOWLEDGEMENTS

Special thanks to Fabrizio Cara, Michele Cercato, Daniela Famiani, Iolanda Gaudiosi, Salomon Hailemikael, Deborah Di Naccio and Gaetano De Luca for their support in the field and constructive comments. GDG was financially supported by Project FIRB – Abruzzo ('Indagini ad alta risoluzione per la stima della pericolosità e del rischio sismico nelle aree colpite dal terremoto del 6 aprile 2009', Research Unit no. 7, http://progettoabruzzo.rm.ingv.it/en, funding code RBAP10ZC8K_007). The work was financially supported in part by Ministero per i Beni e le Attività Culturali (Progetto SISMA Abruzzo – Verifiche di Vulnerabilità sismica) and in part by Ministero dell'Istruzione, dell'Università e della Ricerca (ex 60% grants to PB, GR, FS and GL). We thank the GJI editor Xiaofei Chen and two anonymous reviewers, they helped to improve the manuscript with useful comments. Data collected during this study are available after request to the authors.

REFERENCES

Amoruso, A., Crescentini, L. & Scarpa, R., 1998. Inversion of source parameters from near and far field observations: an application to the 1915 Fucino earthquake, Central Apennines, *J. geophys. Res.,* **103,** 29 989–29 999.

Bard, P.Y. & Bouchon, M., 1980a. The seismic response of sediment-filled valleys. Part 1. The case of incident SH waves, *Bull. seism. Soc. Am.,* **70,** 1263–1286.

Bard, P.Y. & Bouchon, M., 1980b. The seismic response of sediment-filled valleys. Part 2. The case of incident P-SV waves, *Bull. seism. Soc. Am.,* **70,** 1921–1941.

Bard, P.Y. & Bouchon, M., 1985. The two-dimensional resonances of sediment-filled valleys, *Bull. seism. Soc. Am.,* **75**(2), 519–541.

Bard, P.-Y. & SESAME-Team, 2005. Guidelines for the implementation of the H/V spectral ratio technique on ambient vibrations–measurements, processing and interpretations, SESAME European research project EVG1-CT-2000–00026, deliverable D23.12.

Bardet, J.P., Ichii, K. & Lin, C.H., 2000. *EERA, a computer program for equivalent-linear earthquake site response analyses of layered soil deposits, Department of Civil Engineering,* University of Southern California, Available at: http://gees.usc.edu/GEES/.

Bindi, D. *et al.*, 2009. Site Amplifications Observed in the Gubbio Basin, Central Italy: hints for lateral propagation effects, *Bull. seism. Soc. Am.,* **99,** 741–760.

Boncio, P., Lavecchia, G. & Pace, B., 2004. Defining a model of 3D seismogenic sources for Seismic Hazard Assessment applications: the case of central Apennines (Italy), *J. Seismol.,* **8**(3), 407–425.

Boncio, P., Pizzi, A., Brozzetti, F., Pomposo, G., Lavecchia, G., Di Naccio, D. & Ferrarini, F., 2010. Coseismic ground deformation of the 6 April 2009 L'Aquila earthquake (central Italy, Mw6. 3), *Geophys. Res. Lett.,* **37**(6).

Boncio, P. *et al.*, 2011. Geological and geophysical characterisation of the Paganica-San Gregorio area after the April 6, 2009 L'Aquila earthquake (Mw 6.3, central Italy): implications for site response, *Boll. Geofis. Teor. Appl,* **52,** 491–512.

Bonnefoy-Claudet, S., 2004. Nature du bruit de fond sismique: implications pour les études des effets de site, *PhD thesis,* Université Joseph-Fourier-Grenoble I, France.

Bonnefoy-Claudet, S., Cornou, C., Bard, P.Y., Cotton, F., Moczo, P., Kristek, J. & Fäh, D., 2006. H/V ratio: a tool for site effects evaluation. Results from 1-D noise simulations, *Geophys. J. Int.,* **167,** 827–837.

Bonnefoy-Claudet, S., Baize, S., Bonilla, L. F., Berge-Thierry, C., Pasten, C., Campos, J., Volant, P. & Verdugo, R., 2009. Site effect evaluation in the basin of Santiago de Chile using ambient noise measurements, *Geophys. J. Int.,* **176,** 925–937.

Boore, D., 2003. Simulation of ground motion using the stochastic method, *Pure appl. Geophys.,* **160,** 635–676.

Capon, J., 1969. High-resolution frequency-wavenumber spectrum analysis, *Proc. IEEE,* **57,** 1408–1418.

Cara, F., Di Giulio, G., Cavinato, G.P., Famiani, D. & Milana, G., 2011. Seismic characterization and monitoring of Fucino Basin (Central Italy), *Bull. Earthq. Eng.,* **9**(6), 1961–1985.

Carta Geologica d'Italia, 2005. Foglio 369 Sulmona, scala **1**:50. 000, APAT (Servizio Geologico d'Italia) and Regione Abruzzo.

Castellaro, S. & Mulargia, F., 2009a. Vs30 estimates using constrained H/V measurements, *Bull. seism. Soc. Am.,* **99,** 761–773 .

Castellaro, S. & Mulargia, F., 2009b. The effect of a velocity inversion on H/V, *Pure appl. Geophys.,* **166,** 567–592.

Ceccaroni, E., Ameri, G., Gómez Capera, A.A. & Galadini, F., 2009. The 2nd century AD earthquake in Central Italy: archaeo-seismological data and seismotectonic implications, *Natural Hazards,* **50,** 335–359.

Centamore, E. *et al.*, 2006. Note illustrative della Carta Geologica d'Italia alla scala 1:50.000, Foglio 359 "L'Aquila", APAT – Servizio Geologico d'Italia e Regione Abruzzo – Servizio Difesa del Suolo, S.EL.CA., Firenze.

Chaljub, E., 2006. Spectral-element modeling of 3D wave propagation in the alpine valley of Grenoble, France, in *Third International Symposium on the Effects of Surface Geology on Seismic Motion,* Grenoble, France, 30 August - 1 September 2006, Paper Number S04.

Chaljub, E., Komatitsch, D., Vilotte, J.P., Capdeville, Y., Valette, B. & Festa, G., 2007. Spectral-element analysis in seismology, in *Advances in Wave Propagation in Heterogeneous Media,* Vol. 48 of *Advanced in Geophysics,* pp. 365–419, eds Wu, R.-S. & Maupin, V., Elsevier-Academic Press.

Chaljub, E., Moczo, P., Tsuno, S., Bard, P., Kristek, J., Kaser, M., Stupazzini, M. & Kristekova, M., 2010. Quantitative comparison of four numerical predictions of 3D ground motion in the Grenoble Valley, France, *Bull. seism. Soc. Am.,* **100**(4), 1427–1455.

Cupillard, P., Delavaud, E., Burgos, G., Festa, G., Vilotte, J.P., Capdeville, Y. & Montagner, J.P., 2012. RegSEM: a versatile code based on the spectral element method to compute seismic wave propagation at the regional scale, *Geophys. J. Int.,* doi:10.1111/j.1365-246X.2011.05311.x.

D'Agostino, N. *et al.*, 2011. Evidence for localized active extension in the central Apennines (Italy) from global positioning system observations, *Geology,* **39**.4, 291–294.

de Nardis, R. *et al.*, 2011. A temporary seismic monitoring of the sulmona area (Abruzzo, Italy) for seismotectonic purposes, *Boll. Geof. Teor. Appl.,* **52,** 651–666.

Di Capua, G., Peppoloni, S. & Manuel, M.R., 2009. Microzonazione sismica speditiva del centro storico di Sulmona (AQ), Available at: http://www.earth-prints.org/handle/2122/5687 (in Italian).

Di Filippo, M. & Miccadei, E., 1997. Analisi gravimetriche della Conca di Sulmona, *Il Quaternario,* **10,** 483–486.

Di Giulio, G., Cornou, C., Ohrnberger, M., Wathelet, M. & Rovelli, A., 2006. Deriving wavefield characteristics and shear-velocity profiles from two-dimensional small-aperture array analysis of ambient vibrations in a small-size alluvial basin, Colfiorito, Italy, *Bull. seism. Soc. Am.,* **96**(5), 1915–1933.

Di Giulio, G. *et al.*, 2012. Exploring the model space and ranking a best class of models in surface-wave dispersion inversion: application at European strong-motion sites, *Geophysics,* **77**(3), B147–B166.

Endrun, B., Ohrnberger, M. & Savvaidis, A., 2010. On the repeatability and consistency of three-component ambient vibration array measurements, *Bull. Earthq. Eng.,* **8,** 535–570.

Faccioli, E., Stupazzini, M., Galadini, F. & Gori, S., 2008. S2-Project: Near-fault earthquake ground motion simulation in the Sulmona alluvial basin, in *AGU Fall Meeting Abstracts* (Vol. **1,** p. 1937, Abstract S33A-1937).

Fäh, D., Kind, F. & Giardini, D., 2001. A theoretical investigation of average H/V ratios, *Geophys. J. Int.,* **145**(2), 535–549.

Ferrarini, F., Lavecchia, G., de Nardis, R. & Brozzetti, F., 2014. Fault geometry and active stress from earthquakes and field geology data analysis: the Colfiorito 1997 and L'Aquila 2009 Cases (Central Italy), *Pure appl. Geophys.,* 1–25.

Fichtner, A., 2011. Full seismic waveform modelling and inversion, in *Advances in Geophysical and Environmental Mechanics and Mathematics,* Series Editor Prof. Kolumban Hutter, Springer, 343 pp.

Forbriger, T., 2003. Inversion of shallow-seismic wavefields: II. Inferring subsurface properties from wavefield transforms, *Geophys. J. Int.,* **153,** 735–752.

Galadini, F. & Galli, P., 2000. Active tectonics in the Central Apennines (Italy)—input data for seismic hazard assessment, *Nat. Hazard,* **22,** 225–270.

Galli, P., Giaccio, B., Peronace, E. & Messina, P., 2015. Holocene Paleoearthquakes and Early-Late Pleistocene slip rate on the Sulmona Fault (Central Apenines, Italy), *Bull. seism. Soc. Am.,* **105**(1), 1–13.

Gallipoli, M.R., Albarello, D., Mucciarelli, M. & Bianca, M., 2011. Ambient noise measurements to support emergency seismic microzonation: the Abruzzo 2009 earthquake experience, *Boll. Geof. Teor. Appl.,* **52,** 539–559.

Gao, S., Liu, H., Davis, P.M. & Knopoff, L., 1996. Localized amplification of seismic waves and correlation with damage due to the Northridge earthquake: evidence for focusing in Santa Monica, *Bull. seism. Soc. Am.,* **86**(1B), S209–S230.

Geoplanning, 1999. Abbazia di S. Spirito al Morrone—Sulmona (AQ), Indagini geognostiche e geotecniche, Unpublished professional report, 8 pp, 4 Annexes.

Giaccio, B. *et al.*, 2012. Fault and basin depocentre migration over the last 2 Ma in the L'Aquila 2009 earthquake region, central Italian Apennines, *Quarter. Sci. Rev.,* **56,** 69–88.

Gori, S., Giaccio, B., Galadini, F., Falcucci, E., Messina, P., Sposato, A. & Dramis, F., 2011. Active normal faulting along the Mt. Morrone south-western slopes (central Apennines, Italy), *Int. J. Earthq. Sci. (Geol Rundsch),* **100,** 157–171.

Gorini, A. *et al.*, 2010. The Italian strong motion network, *Bull. Earthq. Eng.,* **8**(5), 1075–1090.

Guidoboni, E., Ferrari, G., Mariotti, D., Comastri, A., Tarabusi, G. & Valensise, G., 2007. CFTI4Med. *Catalogue of Strong Earthquakes in Italy (461 BC-1997) and Mediterranean Area (760 BC-1500). INGV-SGA*. Available at: http://storing.ingv.it/cfti4med.

Herrmann, R.B. & Ammon, C.J. 2002. Computer Programs in Seismology, version 3.20: Surface Waves, *Receiver Functions, and Crustal Structure,* St. Louis University, Missouri.

Hobiger, M. *et al.*, 2013. Ground structure imaging by inversions of Rayleigh wave ellipticity: sensitivity analysis and application to European strong-motion sites, *Geophys. J. Int.,* **192**(1), 207–229.

Kawase, H., 1996. The cause of the damage belt in Kobe: "the basin edge effect," constructive interference of the direct S-wave with the basin induced diffracted/Rayleigh waves, *Seism. Res. Lett.,* **67**(6), 25–34.

Komatitsch, D. & Vilotte, J.P., 1998. The spectral element method: an efficient tool to simulate the seismic response of 2D and 3D geological structure, *Bull. seism. Soc. Am.,* **88**(2), 368–392.

Komatitsch, D. & Tromp, J., 1999. Introduction to the spectral element method for three-dimensional seismic wave propagation, *Geophys. J. Int.,* **139,** 806–822.

Komatitsch, D. & Tromp, J., 2002. Spectral-element simulations of global seismic wave propagation, part II: 3D models, oceans, rotation and gravity, *Geophys. J. Int.,* **150,** 303–318.

Konno, K. & Ohmachi, T., 1998. Ground-motion characteristics estimated from spectral ratio between horizontal and vertical components of microtremor, *Bull. seism. Soc. Am.,* **88,** 228–241.

Lavecchia, G. & de Nardis, R., 2009. Seismogenic sources of major earthquakes of the Maiella area (Central Italy): constraints from macroseismic field simultaions and regional seimotectonics, UR 4.01-S1-29, Poster at the INGV-DPC meeting, Rome, November.

Lavecchia, G., Ferrarini, F., Brozzetti, F., de Nardis, R., Boncio, P. & Chiaraluce, L., 2012. From surface geology to aftershock analysis: constraints on the geometry of the L'Aquila 2009 seismogenic fault system, *Italian J. Geosci.,* **131,** 330–347.

Lee, S.J., Komatitsch, D., Huang, B.S. & Tromp, J., 2009. Effects of topography on seismic-wave propagation: an example from Northern Taiwan, *Bull. seism. Soc. Am.,* **99**(1), 314–325.

Lunedei, E. & Albarello, D., 2010. Theoretical HVSR curves from full wavefield modeling of ambient vibrations in a weakly dissipative layered Earth, *Geophys. J. Int.,* **181,** 1093–1108.

Makra, K., Raptakis, D., Chavez.Garcia, F.J. & Pitilakis, K., 2001. Site effects and design provisions: the case of Euroseistest, *Pure appl. Geophys.,* **158,** 2349–2367.

Miccadei, E., Barberi, R. & Cavinato, G.P., 1998. La geologia quaternaria della conca di Sulmona (Abruzzo, Italia centrale), *Geologica Romana,* **34,** 59–86.

Miccadei, E., Piacentini, T. & Barberi, R., 2002. Uplift and local tectonic subsidence in the evolution of intramontane basins: the example of the Sulmona basin (central Appennines, Italy). Large-scale vertical movements and related gravitational processes, in *Proceedings of the International Workshop Camerino-Rome, 1999*. Studi Geologici Camerti, Camerino, pp. 119–134.

MS, Working Group, 2008. Indirizzi e criteri per la microzonazione sismica, in *Conferenza delle Regioni e delle Province autonome-Dipartimento della protezione civile,* Roma. Vol. 3, Cd-rom [in Italian].

MS-AQ Working Group, 2010. Microzonazione sismica per la ricostruzione dell'area aquilana, In Regione Abruzzo-Dipartimento della Protezione Civile, 1–796, Vol. 3, CD-rom [in Italian].

Nakamura, Y., 1989. A method for dynamic characteristics estimation of subsurface using ambient noise on the ground surface, *Q. R. Rail. Tech. Res. Inst.,* **30**(1), 25–33.

NTC, 2008. Norme Tecniche per le Costruzioni, DM 14/01/2008, in *GU n.29 del 04/02/2008, Suppl. Ord. 30* (in Italian).

Ohrnberger, M., Schissele, E., Cornou, C., Bonnefoy-Claudet, S., Wathelet, M., Savvaidis, A., Scherbaum, F. & Jongmanns, D., 2004. Frequency wavenumber and spatial autocorrelation methods for dispersion curve determination from ambient vibration recordings, in *Proceedings of the 13th World Conference on Earthquake Engineering,* Vancouver, Canada, paper no. 946.

Ordaz, M., Arboleda, J. & Singh, S.K., 1995. A scheme of random summation of an empirical Green's function to estimate ground motions from future large earthquakes, *Bull. seism. Soc. Am.,* **85**(6), 1635–1647.

Picozzi, M., Parolai, S., Bindi, D. & Strollo, A., 2009. Characterization of shallow geology by high-frequency seismic noise tomography, *Geophys. J. Int.,* **176,** 164–174.

Pondrelli, S., Salimbeni, S., Ekström, G., Morelli, A., Gasperini, P. & Vannucci, G., 2006. The Italian CMT dataset from 1977 to the present, *Phys. Earth planet. Inter.,* **159**(3), 286–303.

Pondrelli, S., Salimbeni, S., Morelli, A., Ekström, G., Olivieri, M. & Boschi, E. 2010. Seismic moment tensors of the April 2009, L'Aquila (Central Italy), earthquake sequence, *Geophys. J. Int.,* **180,** 238–242.

Renalier, F. & Endrun, B., 2009. Comparative analysis of classical measurements and newly developed methods, NERIES project JRA4 Task C, EU-FP6 EC project number 026130, deliverable D6, Available at: via http://www.neries-eu.org/?subpage = /projectweb/portalproject/Deliverables.html, accessed 28 December 2011.

Renalier, F., 2010. Caractérisation sismique de sites hétérogènes à partir de méthodes actives et passives: variations latérales et temporelles, *PhD thesis*, Université Joseph-Fourier-Grenoble I.

Renalier, F., Jongmans, D., Campillo, M. & Bard, P.Y., 2010. Shear wave velocity imaging of the Avignonet landslide (France) using ambient noise cross correlation, *J. geophys. Res.,* **115,** F03032, doi:10.1029/2009JF001538.

Romano, M.A., de Nardis, R., Garbin, M., Peruzza, L., Priolo, E., Lavecchia, G. & Romanelli, M., 2013. Temporary seismic monitoring of the sulmona area (Abruzzo, Italy): a quality study of microearthquake locations, *Nat. Hazards Earth Syst. Sci.,* **13,** 2727–2744.

Roten, D., Fäh, D., Cornou, C. & Giardini, D., 2006. Two-dimensional resonances in Alpine valley identified from ambient vibration wavefield, *Geophys. J. Int.,* **165,** 889–905.

Rovida, A., Camassi, R., Gasperini, P. & Stucchi, M., 2011. CPTI11, la versione 2011 del Catalogo Parametrico dei Terremoti Italiani, Milano, Bologna.

Sambridge, M., 1999. Geophysical inversion with a neighbourhood algorithm: I. Searching a parameter space, *Geophys. J. Int.,* **138,** 479–494.

Scherbaum, F., Hinzen, K.G. & Ohrnberger, M., 2003. Determination of shallow shear wave velocity profiles in the Cologne/Germany area using ambient vibrations, *Geophys. J. Int.,* **152,** 597–612.

Semblat, J.F., Kham, M., Parara, E., Bard, P.Y., Pitilakis, K., Makra, K. & Raptakis, D., 2005. Site effects: basin geometry vs soil layering, *Soil Dyn. Earthq. Eng.,* **25**(7–10), 529–538.

Smerzini, C., Paolucci, R. & Stupazzini, M., 2011. Comparison of 3D, 2D and 1D numerical approaches to predict long period earthquake ground motion in the Gubbio plain, Central Italy, *Bull. Earthq. Eng.,* **9,** 2007–2029.

Socco, L.V., Foti, S. & Boiero, D., 2010. Surface-wave analysis for building near-surface velocity models—established approaches and new perspectives, *Geophysics,* **75**(5), 75A83–75A102.

Steimen, S., Fäh, D., Kind, F., Schmid, C. & Giardini, D., 2003. Identifying 2D resonance in microtremor wave fields, *Bull. seism. Soc. Am.,* **93**(2), 583–599.

Stupazzini, M., 2004. A spectral element approach for 3D dynamic soil-structure interaction problems, *PhD thesis,* Politecnico di Milano, Italy.

Stupazzini, M., Smerzini, C., Cauzzi, C., Faccioli, E., Galadini, F. & Gori, S., 2009a. The Italian Project S2-Task 4: Near-fault earthquake ground motion simulation in the Sulmona alluvial basin, in *Proceedings of the EGU General Assembly Conference Abstracts* (Vol. 11, p. 12102).

Stupazzini, M., Paolucci, R. & Igel, H., 2009b. Near-Fault Earthquake Ground-Motion Simulation in the Grenoble Valley by a High-Performance Spectral Element Code, *Bull. seism. Soc. Am.,* **99**(1), 286–301.

Tatoni, S., 2011. Progetto definitivo per gli interventi di miglioramento sismico relativo alla Chiesa annessa all'Abbazia di S. *Spirito al Morrone, Relazione geologica e sismica,* Unpublished professional report, 174 pp.

Tokimatsu, K., 1997. Geotechnical site characterization using surface waves, in *Proceedings IS-Tokyo 95, The First International Conference on Earthquake Geotechnical Engineering,* pp. 1333–1368, eds Ishihara, K. & Balkema, A.A., Rotterdam, The Netherlands.

Uebayashi, H. 2003. Extrapolation of irregular subsurface structures using the Horizontal-to-vertical spectra ratio of long-period microtremors, *Bull. seism. Soc. Am.,* **93**(2), 570–582.

Villani, M., Faccioli, E., Ordaz, M. & Stupazzini, M., 2013. High resolution seismic hazard analysis in a complex geological configuration: the case of Sulmona (Central Italy) basin, *Earthq. Spectra,* doi: http://dx.doi.org/10.1193/112911EQS288M.

Wathelet, M., 2005. Array recordings of ambient vibrations: surface-wave inversion, *PhD thesis,* University de Liège, Liège, Belgium, Available at: http://marc.geopsy.org/publications.html.

Wathelet, M., 2008. An improved neighborhood algorithm: parameter conditions and dynamic scaling, *Geophys. Res. Lett.,* **35,** L09301, doi:10.1029/2008GL033256.

Wathelet, M., Jongmans, D., Ohrnberger, M. & Bonnefoy-Claudet, S., 2008. Array performances for ambient vibrations on a shallow structure and consequences over Vs inversion, *J. Seismol.,* **12,** 1–19.

Xia, J., Miller, R.D. & Park, C.B., 1999. Estimation of near-surface shear-wave velocity by inversion of Rayleigh waves, *Geophysics,* **64**(3), 691–700.

Zambonelli, E., de Nardis, R., Filippi, L., Nicoletti, M & Dolce, M., 2011. Performance of the Italian strong motion network during the 2009, L'Aquila seismic sequence (central Italy), *Bull. Earthq. Eng.,* **9**(1), 39–65.

SUPPORTING INFORMATION

Additional Supporting Information may be found in the online version of this paper:

Figure S1. Variation in the stiffness decay G/G_{max} and damping D curves with different shear strains (γ) used in the 1-D numerical analyses. Non-linear behaviour of the gravel (a) from the MS Working Group (2008), the silty clay/clayey silt (b) from laboratory tests (this study), and the silty sand (c) and white lacustrine silt (d) from the MS-AQ Working Group (2010).

Figure S2. Snapshot of the wavefield (at a generic time *t*) that was generated by a Dirac source in the soft layer at the left of the model, which is characterized by an uppermost stiff layer (*stiff model*). The

computational domain was 2000·900 m (x, z); the Dirac source was initially situated at the point with coordinates 200, 875 m.

Figure S3. Synthetics for the *stiff model* (top) and the *soft model* (bottom). The synthetics refer to a receiver located at $x = 798$ m (receiver number 120). The horizontal x component is shown on the left-hand panel, the vertical z component is on the right-hand panel.

Figure S4. Stack of the time-series of the synthetics (for 5 s of simulation) for the *stiff model* (top) and *soft model* (bottom). The horizontal component is shown on the left-hand panel, and the vertical component is shown on the right-hand panel.

Table S1. Characteristics of the silty clay/clayey silt in terms of the stiffness decay (G/G_{max}) and damping curves with different shear strain (Fig. S1b). The curves are derived from a cyclic, dynamic laboratory test (resonant column) on an undisturbed borehole sample. (http://gji.oxfordjournals.org/lookup/suppl/doi:10.1093/gji/ggv444/-/DC1).

Please note: Oxford University Press is not responsible for the content or functionality of any supporting materials supplied by the authors. Any queries (other than missing material) should be directed to the corresponding author for the paper.